https://doi.org/10.5194/egusphere-2026-3724
Preprint. Discussion started: 27 July 2026

Large-scale atmospheric drivers of recent hydroclimatic changes in the Horn of Africa: evidence from the Awash Basin terminal lake system, Ethiopia

Juan P. Sierra[1,2], Pierre Brigode[2], Pape Saara Ngom[2], Pascale Braconnot[3], Christian Le Carlier De Veslud[2], Camille Bouchez[2], Sly Wongchuig[4], Mohamed Osman Awaleh[5], Mohamed Jalludin[5], Natacha Volto[6], Eric Chaumillon[6], and Marie Revel[1]

[1]Géoazur, Université Côte d'Azur, CNRS, OCA, IRD, Valbonne, 06152, France
[2]Univ Rennes, CNRS, Géosciences Rennes, UMR 6118, 35000 Rennes, France
[3]Laboratoire des Sciences du Climat et de l'Environnement, Institut Pierre-Simon Laplace UMR CEA, CNRS, UVSQ, Université Paris-Saclay, Gif-sur-Yvette, 91190, France
[4]Université de Toulouse, LEGOS, CNES/CNRS/IRD/UT, Toulouse, France
[5]Institut des Sciences de la Terre, Centre d'Etudes et de Recherches de Djibouti (CERD), Route de l'aéroport B.P. 486, Djibouti, ville, Republic of Djibouti.
[6]La Rochelle Université, CNRS, UMR 7266 LIENSs, La Rochelle, France

Correspondence: Juan P. Sierra (juanpablosierrap@gmail.com)

Abstract. The Horn of Africa, and specifically Ethiopia's Awash Basin, is experiencing accelerating hydroclimatic change, yet the mechanisms driving multi-decadal shifts in its regional water balance remain poorly understood. The terminal Afambo–Gemeri–Abhe lake system, an endorheic water body at the outlet of the Awash Basin, acts as a natural integrator of its catchment's net water balance, providing a sensitive record of regional atmospheric dynamics. This study reconstructs its hydrological history over 1985–2024 by coupling the GR2M hydrological model with a lake water-balance model, constrained by satellite observations and in situ data. The model reproduces observed lake surface area dynamics and reliably extends the record into the data-scarce pre-1998 period allowing us to relate recent lake surface area changes to large scale circulation variability and trends.

The reconstructed history reveals two superimposed signals. The first is pronounced variability across interannual to interdecadal timescales, driven by the El Niño–Southern Oscillation (ENSO), the Pacific Decadal Oscillation (PDO), and the Subtropical Indian Ocean Dipole (SIOD). The second is a non-oscillatory, multi-decadal expansion: the lake tripled in surface area from $\sim$150 km^2 in the 1980s to $\sim$450 km^2 by 2024, with growth accelerating markedly after 2020. This systematic expansion reflects a reorganization of the regional water balance driven by increased July–September rainfall and changes in potential evapotranspiration. We attribute these basin-scale changes to large-scale atmospheric circulation shifts, including a strengthening of the Somali Jet, the Tropical Easterly Jet, and the Indian monsoon circulation, and a northward shift of the Intertropical Convergence Zone and of the African Easterly Jet, likely linked to amplified regional warming over the Arabian Peninsula and the Tibetan Plateau. This modelling framework provides a transferable tool for evaluating past and future hydroclimatic variability, supporting more robust water resource assessments in data-scarce regions.

https://doi.org/10.5194/egusphere-2026-3724
Preprint. Discussion started: 27 July 2026

1 Introduction

The Horn of Africa is one of the region most vulnerable to climate variability and change, characterized by strong rainfall variability and recurrent droughts and floods, with major impacts on water resources, agriculture, and livelihoods (Pörtner et al., 2022). Droughts are the most frequent hazard and the primary driver of food insecurity and poverty in the region (Qu et al., 2019; FAO, 2023), with several studies reporting an increase in drought frequency over recent decades. This trend is largely attributed to declining rainfall during the March–April–May (MAM) season (Funk et al., 2008; Williams and Funk, 2011), driven by a combination of anthropogenic climate change (Tierney et al., 2015) and internal climate variability and ocean–atmosphere interactions (Lyon et al., 2014; Lyon and DeWitt, 2012; Yang et al., 2014). In contrast, the October–December season has shown a positive rainfall trend (Palmer et al., 2023). These opposing seasonal trends have important implications for regional hydrology and water availability.

The vulnerability of the Horn of Africa is further exacerbated by socio-economic factors, including dependence on rain-fed agriculture (Alfieri et al., 2024; World Bank Group, 2023), reliance on hydropower for energy production (Conway et al., 2017), and rapid population growth (United Nations, 2022). Ethiopia exemplifies this vulnerability: approximately 67% of its population is employed in agriculture (World Bank Group, 2023) and about 88% of its electricity depends on hydropower (Degefu et al., 2015), making interannual climate variability a direct threat to livelihoods and the national economy. Recurrent droughts occur every 4–10 years (Abate, 1994; Wolde-Georgis, 1997), while nearly 80% of annual rainfall falls between June and September as intense convective events (Billi et al., 2015; Nicholson, 2017), making large parts of the country also highly prone to flooding (Mamo et al., 2019; Nigusse and Adhanom, 2019; Ogato et al., 2020).

Historical records illustrate the severity of these extremes. The 1984–1985 drought caused an estimated 450,000 fatalities across Ethiopia and Sudan (Vicente-Serrano et al., 2012), and subsequent droughts in 1987–1994, 1999, and 2002 severely impacted agriculture and the economy (Edossa et al., 2010). In 2015, a strong El Niño combined with a delayed onset of the February–May rains reduced annual precipitation to 50–75% of the climatological mean (Philip et al., 2018; Singh et al., 2016), and the 2022 drought caused the death of approximately 2.2 million livestock (FEWS NET, 2023). These events reflect a broader trend toward increasing drought frequency and severity, particularly in central and northern Ethiopia (Mulualem et al., 2024; Di Nunno et al., 2025). Flooding, often associated with La Niña conditions (Abtew et al., 2009; Mamo et al., 2019), has also intensified: the spatial extent of flood-affected areas rose from 0.7% in the 1960s to 16.7% in the 1990s and has continued to increase since (Billi et al., 2015; Mamo et al., 2019), with the 2020 floods alone displacing more than 30,000 people (Melkamu et al., 2022).

Observed trends in droughts and floods are broadly consistent with climate projections under global warming, which indicate more frequent extreme rainfall events and more severe droughts (Finney et al., 2020; Haile et al., 2020; Hirpa et al., 2019; Richardson et al., 2022). Placing these recent changes in a longer-term perspective requires records extending beyond the instrumental period. Lakes within the Ethiopian Rift System — positioned between humid highlands and arid lowlands — serve as valuable natural archives for this purpose, being highly sensitive to hydroclimatic fluctuations and responding rapidly to water balance changes (Maslin et al., 2014; Okech et al., 2019). Lacustrine sediment records have therefore been widely

https://doi.org/10.5194/egusphere-2026-3724
Preprint. Discussion started: 27 July 2026

used to reconstruct past climate variability and place recent changes in a longer-term perspective (Hastenrath, 2001; Mologni et al., 2024; Schaebitz et al., 2021).

Within this context, the Awash Basin represents a key socio-economic and hydrological system. Located in central Ethiopia and extending toward Djibouti, it covers approximately 112,700 km^2 with elevations ranging from 4,195 m to 250 m a.s.l., forming an endorheic system that terminates at the Afambo–Gemeri–Abhe lake system on the Ethiopian–Djiboutian border (Fig. 1a; Tilahun et al., 2025). The basin is home to approximately 16.3 million people ($\sim$17% of the national population; Abebe et al., 2025; Awash Basin Authority, 2017), hosts more than 65% of the country's industries, and contains the largest area of irrigated agriculture in Ethiopia (Gemechu et al., 2025; Kidane et al., 2014; Taye et al., 2018). It also plays a central role in hydropower generation and domestic water supply (Malede et al., 2024). The Awash River flows approximately 1,250 km from its source near Ginchi ($\sim$3,000 m a.s.l.) to its terminal lakes ($\sim$250 m a.s.l.; Taddese et al., 2009). Given its exposure to recurrent droughts and floods, understanding hydroclimatic variability in the Awash Basin is of critical importance.

Rainfall in the basin is highly seasonal, with a minor rainy season during MAM and a dominant one during June–September (JJAS), accounting for 50–80% of annual precipitation (Nicholson, 2017), with higher amounts over mountainous areas (Krivoguz et al., 2025). As a result, the basin exhibits strong hydroclimatic contrasts: highlands receive more rainfall and lower potential evaporation than lowlands (Figs. 1b–e), with rainfall exceeding potential evaporation only during MAM and JJAS, primarily above $\sim$3,250 m a.s.l. and $\sim$1,500 m a.s.l., respectively. These conditions control groundwater recharge and runoff generation, leading to peak river discharge between August and September (Fig. 2; Tadese et al., 2019).

Despite its importance, the coupled dynamics linking large-scale climate variability, regional hydroclimate, and lake system responses in the Afar Rift remain poorly constrained. Previous studies have examined atmospheric drivers and hydrological responses largely in isolation. Tarkegn and Jury (2020) linked enhanced moisture transport from South Sudan to strengthened late-season rainfall and associated hydrological changes, but without explicitly quantifying the coupling between atmospheric processes and surface hydrology. Mologni et al. (2024) reconstructed the recent evolution of the Afambo–Gemeri lake system from laminated sediments and identified connections with large-scale climate modes such as ENSO, yet the underlying atmospheric mechanisms remain insufficiently characterized. Addressing this gap requires an integrated framework combining hydrological modelling with a process-based analysis of climate drivers.

Here, we investigate the hydroclimatic variability of the Afambo–Gemeri–Abhe lake system at the terminal end of the Awash Basin over the 1985–2024 period. This lacustrine system acts as a natural integrator of basin-scale hydrological variability, as changes in lake storage reflect the cumulative balance of upstream inflows and climatic forcing. To constrain the lake geometry used in model parameterization, we draw on water depth data from sediment coring locations in lakes Afambo, Gemeri, and Abhe, sampled as part of the NILAFAR project — an initiative aimed at reconstructing hydrological fluctuations over the last 20,000 years in north-east Africa. We couple a hydrological model with a lake water-balance model to simulate changes in lake surface area, and by linking the resulting lake dynamics to atmospheric and oceanic variability, we identify the large-scale climate processes that govern hydroclimatic conditions in the Awash Basin.

The paper is organized as follows. Section 2 describes the datasets, hydrological model, and methodological framework. Section 3 presents the results, including the reconstruction of lake system dynamics (Sect. 3.1–3.2), the identification of major

https://doi.org/10.5194/egusphere-2026-3724
Preprint. Discussion started: 27 July 2026

teleconnections and oceanic drivers (Sect. 3.3), and the analysis of large-scale and regional shifts (Sect. 3.4). Conclusions and perspectives are provided in Sect. 4.

2 Methods

2.1 Data

This section describes the datasets used to characterise the hydrology of the Awash Basin and to investigate its relationship with large-scale climate drivers.

2.1.1 Rainfall

Daily precipitation data were obtained from three high-resolution satellite products. The primary dataset was CHIRPS v2.0 (Funk et al., 2015), providing quasi-global daily estimates at 0.05° (∼5 km) resolution from 1981 to present (50°N–50°S), combining satellite infrared observations with station data. CHIRPS has been shown to reliably capture rainfall variability over eastern Africa, particularly in Ethiopia (Dinku et al., 2018; Wedajo et al., 2021). To assess temporal rainfall evolution in the Awash Basin, two additional products were used: CMORPH v1.0 (Joyce et al., 2004), offering 3-hourly estimates at 0.25° from 1998 onwards based on microwave observations propagated using infrared imagery; and TRMM 3B42 v7 (Huffman et al., 2007), providing gauge-corrected 3-hourly estimates at 0.25° for 1998–2019.

2.1.2 Land evapostranspiration

Actual and potential evapotranspiration were obtained from GLEAM v4.2a (Miralles et al., 2025), which provides daily estimates at 0.1° (∼10 km) resolution for 1980–2025. Actual evapotranspiration is derived by scaling potential evapotranspiration — computed via the Penman equation — with a root-zone soil moisture stress factor. GLEAM performs particularly well in semi-arid, water-limited environments such as the Afar Depression (Akpoti et al., 2025). To characterize uncertainty in the atmospheric water balance at the watershed scale arising from differences in input products and model structure, additional evapotranspiration datasets were incorporated. These included output from four global hydrological models contributed to the eartH2Observe intercomparison project (1980–2014; 0.25° resolution): WaterGAP3 (Muller et al., 2021), PCR-GLOBWB (Sutanudjaja et al., 2018), HTESSEL (Balsamo et al., 2009), and LISFLOOD (Knijff et al., 2010). Satellite-based and reanalysis-derived estimates from MODIS16A2 (Running et al., 2017) and CRUv4.09 (Harris et al., 2020) were also included.

2.1.3 Atmospheric data

To analyze atmospheric mechanisms influencing the hydroclimatology of the basin, horizontal and vertical wind components, specific humidity, geopotential height, and air temperature at multiple pressure levels were extracted from the ERA5 reanalysis (Hersbach et al., 2020). ERA5 is a global atmospheric reanalysis produced by the European Centre for Medium-Range Weather Forecasts ECMWF providing hourly estimates at 0.25° (∼31 km) resolution from 1950 to present. Thanks to the assimilation of

https://doi.org/10.5194/egusphere-2026-3724
Preprint. Discussion started: 27 July 2026

observations from satellite radiances, radiosonde measurements, aircraft observations, surface weather stations, ships, drifting buoys, scatterometer winds and radar-derived precipitation observations, it provides physically consistent, gap-free fields.

Monthly mean air temperature was obtained from CRU TS v4.09 (Harris et al., 2020), a gridded global land-surface dataset at 0.5° (∼50 km) resolution spanning 1901 to present, constructed by interpolating an extensive network of station observations onto a regular grid.

2.1.4 Sea surface temperature

Ocean–atmosphere interactions were examined using daily global sea surface temperature (SST) data from OISST v2.1 (0.25° resolution, 1981–present), which combines in situ ship and buoy measurements with satellite observations through statistical interpolation (Huang et al., 2021). Decadal and interannual SST variability were characterized using the monthly PDO index from NOAA/NCEI (https://www.ncei.noaa.gov/access/monitoring/pdo/; last access: 12 February 2026), which represents the leading mode of North Pacific SST variability with positive (negative) values indicating anomalously warm (cold) conditions along the North American west coast relative to the central North Pacific (Zhang et al., 1997), and SST anomalies over the Niño 3, Niño 4, and Niño 3.4 regions derived from the Extended Reconstructed Sea Surface Temperature version 5 dataset (NOAA/NCEI; https://www.cpc.ncep.noaa.gov/data/indices/sstoi.indices; last access: 7 April 2026).

2.1.5 Topographic data

Topographic data were obtained from two sources. The Shuttle Radar Topography Mission (SRTM; Farr et al., 2007) provides near-global elevation data at 30 m resolution using radar interferometry, and was used here in combination with satellite imagery, water depth data from NILAFAR coring sites, and altimetry data to derive hypsometric relationships for Lakes Afambo, Gemeri, and Abhe, and to analyze the distribution of precipitation and potential evaporation with elevation across the Awash Basin. Coarser topographic context was provided by GTOPO30 (Gesch et al., 1999), a global digital elevation model at ∼1 km resolution developed by the USGS from multiple sources, used here to illustrate regional-scale topographic cross-sections along selected transects.

2.1.6 River discharge

Streamflow observations were obtained from the Global Runoff Data Centre (GRDC; https://grdc.bafg.de/, last access: 12 February 2026). Of the 13 available stations within the Awash Basin, the Tendaho station (Fig. 1a) was selected for model calibration and validation, as it is the closest gauge to the Afambo–Gemeri–Abhe lacustrine system and lies at the terminal reach of the endorheic basin.

2.1.7 Lake surface

Surface water extent was obtained from the Global Surface Water Database (GSWD; Pekel et al., 2016), derived from the full Landsat archive at 30 m resolution for 1984–2021. For 2021–2025, surface water detection was extended using Landsat

https://doi.org/10.5194/egusphere-2026-3724
Preprint. Discussion started: 27 July 2026

8 and 9 imagery. Given the sparse Landsat coverage over the Afar Depression prior to 1998 (fewer than 30 months of usable observations), lake surface area reconstructions from Zhao et al. (2022) were also used. These combine GSWD data with static lake boundaries from HydroLAKES (Messager et al., 2016), weighting annual water classifications by long-term monthly mean areas to estimate monthly lake surface dynamics. Lake water levels were obtained from the HydroWeb database, which integrates radar altimetry observations from multiple satellite missions to produce long-duration water surface elevation time series (https://hydroweb.next.theia-land.fr/, last access: 12 February 2026).

2.2 Lake characteristic and lake model

2.2.1 Lake surface time series

Constructing lake surface time series from GSWD data is challenging because approximately one-third of pixels are classified as 'no data' (Mullen et al., 2021), arising from cloud contamination, terrain shadows, and the Scan Line Corrector failure on Landsat 7. To address this, we applied the methodology of Mullen et al. (2021), which converts ternary satellite classifications (wet, dry, no data) into binary (wet/dry) images using a supervised random forest classifier trained on the historical flooding frequency of each pixel (Figure S1 in Supplementary material). The resulting corrected lake surface area time series were used to establish initial conditions for the lake model and to validate its output against satellite observations.

2.2.2 The rainfall-runoff model GR2M

Reconstructing the Afambo–Gemeri–Abhe lake system over the past 40 years requires continuous records of Awash River discharge. However, in situ observations at Tendaho span only 1990–2004 and contain 14% missing data, primarily during 1994–1996 and 2003–2004. To overcome this, discharge was simulated using the GR2M rainfall–runoff model (Mouelhi et al., 2006), a conceptual lumped two-parameter model driven by basin-averaged CHIRPS v2 precipitation and GLEAM potential evapotranspiration. Its parsimonious structure enables robust calibration with limited data, making it well suited for long-term water balance assessments, and has recently been applied in the region to investigate drought and flood variability in the Awash Basin using sediment records from Lakes Gemeri and Afambo (Mologni et al., 2024).

The observed streamflow regime at Tendaho is bimodal, with a minor peak in April (short rains, locally known as "Belg") and a major peak in August (main rains, locally known as Kiremt"; Taye et al. 2018; Fig. 2a). Since GR2M underestimated high flows, simulated values at or above the 90th percentile were multiplied by a factor of two. After correction, the model adequately reproduces the seasonal cycle, though it underestimates April flows and slightly overestimates variability during August–September. Despite the short observational record, the influence of ENSO on interannual variability is evident (Fig. 2b), with flow reductions (increases) during El Niño (La Niña) years such as 1991, 1997, and 2002 (1998–1999), consistent with previous studies (Degefu et al., 2017; Le et al., 2020). GR2M captures both the seasonal cycle and ENSO-driven interannual variability, with simulated and observed time series significantly correlated ($r = 0.72$; KGE = 0.64). The model shows a persistent positive bias of +11.59%, primarily reflecting an overestimation of wet-season flows during anomalously wet years, likely an unintended consequence of the bias correction.

https://doi.org/10.5194/egusphere-2026-3724
Preprint. Discussion started: 27 July 2026

2.2.3 Lakes water balance

An independent monthly water balance was established for each lake in the Afambo–Gemeri–Abhe system, following an approach previously applied to data-scarce endorheic lake systems in Africa (Bouchez et al., 2016):

$$\Delta V_m = \left(P_{\mathrm{Lake},m} - E_{\mathrm{Lake},m}\right) A_m + Q_{\mathrm{In},m} - Q_{\mathrm{Out},m} - G_m \tag{1}$$

where ΔV_m is the change in lake volume during month m ($\mathrm{m}^3\,\mathrm{month}^{-1}$), $P_{\mathrm{Lake},m}$ and $E_{\mathrm{Lake},m}$ are the monthly precipitation and evaporation rates over the lake surface ($\mathrm{m\,month}^{-1}$), A_m is the lake surface area at month m (m^2), $Q_{\mathrm{In},m}$ and $Q_{\mathrm{Out},m}$ are the monthly surface inflows and outflows via the Awash River ($\mathrm{m}^3\,\mathrm{month}^{-1}$), respectively, and G_m is the net monthly groundwater outflow ($\mathrm{m}^3\,\mathrm{month}^{-1}$).

Surface water fluxes were computed by multiplying monthly CHIRPS v2 rainfall and GLEAM potential evaporation rates — spatially averaged over static lake polygons from HydroLAKES — by the time-varying lake area A_m at each monthly time step. The static polygons are therefore used solely to derive spatially representative mean monthly rates (in $\mathrm{mm\,month}^{-1}$), while the dynamic extent of the lake is fully accounted for through A_m. Although using static rather than time-varying polygons for spatial averaging is a simplification, its impact on the derived rates is negligible given the low rainfall and limited spatial variability of the lower Awash Basin, as confirmed by a Monte Carlo sensitivity analysis (Figure S2 in Supplementary material). On the other hand, GLEAM yields a long-term mean annual evaporation of 1691 mm for Lake Abhe, which is likely an underestimate given the lower altitude and more arid conditions of the lower Awash Basin relative to other Awash lakes (e.g., Lake Beseka: $\sim$2485 $\mathrm{mm\,year}^{-1}$; Fig. 1a; Abebe et al., 2025). GLEAM potential evaporation was therefore scaled by a correction factor of 1.5, selected through sensitivity analysis (Figure S3 in Supplementary material), yielding an adjusted long-term mean annual evaporation of $\sim$2537 $\mathrm{mm\,year}^{-1}$ for Lake Abhe.

Lake inflows and outflows were derived from GR2M-simulated discharge at Tendaho, partitioned into two branches supplying the Afambo–Gemeri and Abhe sub-systems. The partitioning coefficients — together with the irrigation abstraction fraction — were estimated dynamically using overlapping 10-year moving windows over 1985–2024, allowing them to vary through time in response to changes in irrigation infrastructure and hydrological regime. For each window, the optimal parameter set was selected by minimizing the mean squared error between modeled and GSWD-derived lake surface areas. Further details on model configuration and calibration are provided in Appendix A.

Groundwater fluxes were considered negligible and omitted from the water balance. In the middle and lower Awash Basin, direct groundwater contributions to surface waters are largely absent, regional groundwater largely bypasses the river system, and isolated thermal springs in the area are not hydraulically connected to the river (Ayenew et al., 2008; Kebede et al., 2021).

Hypsometric relationships linking lake volume, surface area, and water level were constructed from water depth measurements at sediment coring sites in all three lakes within the NILAFAR project (Fig. 1a), complemented by SRTM-based slope interpolation and satellite altimetry data for Lake Abhe (Figure S4 in Supplementary material). These relationships enable conversion between simulated volume changes and surface area time series for comparison with satellite observations.

https://doi.org/10.5194/egusphere-2026-3724
Preprint. Discussion started: 27 July 2026

2.3 Hydroclimatological diagnoses

2.3.1 Synchronicity index between precipitation and potential evaporation

Recent evidence suggests that the temporal synchronicity between precipitation and potential evaporation is more important than potential evaporation alone in explaining interannual flow variability (Andréassian et al., 2025). Following Andréassian et al. (2025), we characterize this synchronicity in the Awash Basin using:

$$\hat{\Lambda}_n = \frac{\sum_{m=1}^{12} \min\left(P_{m,n}, E_{m,n}\right)}{\sqrt{P_n E_n}}\,\bar{P} \tag{2}$$

where m and n denote the calendar month and year, respectively; P is the precipitation and E is the potential evaporation ($\mathrm{mm\,month^{-1}}$ or $\mathrm{mm\,year^{-1}}$). The index $\hat{\Lambda}_n$ ($\mathrm{mm\,year^{-1}}$) quantifies the fraction of annual rainfall temporally coinciding with atmospheric evaporative demand, being higher when the seasonal maxima of P and E are in phase and lower when they are offset.

2.3.2 The Atmospheric water balance

The atmospheric water balance was evaluated using the vertically integrated moisture budget equation:

$$\frac{\partial W}{\partial t} = E_{\mathrm{basin}} - P_{\mathrm{basin}} + C \tag{3}$$

where W is the total column water vapor ($\mathrm{kg\,m^{-2}}$), P_{basin} is the basin precipitation, E_{basin} is the basin evapotranspiration (both in $\mathrm{kg\,m^{-2}s^{-1}}$, and C is the vertically integrated horizontal moisture flux convergence ($\mathrm{kg\,m^{-2}s^{-1}}$). Moisture flux convergence and column-integrated moisture transport were computed from ERA5 winds and specific humidity integrated between 1000 and 200 hPa using centered finite differences, following standard formulations (e.g. Wongchuig et al., 2025). Precipitation (CHIRPS v2, CMORPH, TRMM 3B42) and evapotranspiration (WaterGAP3, PCR-GLOBWB, HTESSEL, LISFLOOD, MODIS16A2) were drawn from multiple independent products to assess dataset-related uncertainties in the atmospheric water budget.

2.3.3 Tracking the latitude of the regional Intertropical Convergence Zone (ITCZ)

The ITCZ position over the Horn of Africa was assessed using the precipitation-weighted mean latitude (precipitation centroid) of Adam et al. (2016), computed from zonally averaged precipitation integrated meridionally from 20°S to 20°N and zonally between 20°E and 40°E, with cosine area weighting.

3 Results and discussion

3.1 The Afambo-Gemeri-Abhe lacustric system over the last 40 years

As the terminal sink of the Awash Basin, variations in the Afambo–Gemeri–Abhe combined surface area reflect net water inputs from the basin. The reconstructed lake surface dataset of Zhao et al. (2022) and the lake model provide continuous information

https://doi.org/10.5194/egusphere-2026-3724
Preprint. Discussion started: 27 July 2026

over 1985–2025 using two complementary approaches, particularly valuable before 1998 when satellite observations over the region were scarce.

The lake model reproduces the observed interannual variability of lake surface area with reasonable skill, yielding a Nash–Sutcliffe efficiency of 0.637, a Pearson correlation of 0.85, and a Kling–Gupta efficiency of 0.81, with a small positive bias of +15.54 km^2 (+4.34% relative bias).

All datasets indicate that the lake system remained at relatively low levels during 1985–1995 (Fig. 3a), though with notable differences in the estimated magnitude across products. Independent evidence from laminated sediments in Lakes Gemeri and Afambo confirms dry conditions and high evaporation between 1991 and 1997 (Mologni et al., 2024). Despite these differences, all datasets consistently show a marked increase in lake storage between 1996 and 2002, during which the lake system almost doubled in size.

Between 2002 and 2011, lake levels exhibited marked interannual fluctuations, with peaks in 2002, 2008, and 2011 and minima in 2006 and 2010, which are well represented in the lake model. The associated changes in lake surface area are smaller than those observed between the 1980s and 1990s but occur over much shorter time scales (1–3 years). This shift toward more rapid fluctuations is consistent with reported intensification of hydroclimatic variability in the region (Kobe, 2023; Teku and Eshetu, 2024; Viste et al., 2013).

Between 2012 and 2019, lake surface area declined, with Lake Abhe reaching levels comparable to those of the late 1980s (Figure S5 in Supplementary material), consistent with severe droughts reported in northern Ethiopia during 2015–2017 (Mekonnen and Gokcekus, 2020; Philip et al., 2018). This declining trend was interrupted by two abrupt increases in lake level in 2020 and 2024. The 2020 wet season was exceptionally strong, resulting from the alignment of the 2020–2021 La Niña and the negative phase of the Indian Ocean Dipole (Cullis and Bogale, 2024), and caused severe flooding across several Ethiopian regions including Afar (Melkamu et al., 2022). Similarly, 2024 was among the wettest years on record globally, with extremely high rainfall in East Africa between April and May (Green et al., 2025; Zhang et al., 2025), triggering severe flash floods in the region (Mabumbo et al., 2024) consistent with the rapid lake expansion observed that year. The resulting expansion of Lake Abhe since 2018 is consistent with previous findings based on Sentinel-2 imagery (Liao et al., 2025). However, the lake model underestimates the magnitude of the rapid surface area increases recorded in 2020 and 2024. We attribute this bias to two compounding structural limitations. First, the monthly time step of GR2M precludes explicit representation of short-duration flash flood responses, which drove much of the observed lake expansion in both years. Second, GR2M tends to underestimate streamflow during MAM, which is particularly relevant for 2024 given that the exceptional rainfall was concentrated in this season, likely amplifying the model's inability to capture the observed lake expansion that year.

Satellite observations reveal a trend toward increased hydrological variability and wetter conditions in the lake system. Together, the lake extent contours for 1986, 2001, 2011, 2021, and 2024 illustrate the gradual expansion of the lake system over the past four decades, with the most pronounced growth occurring after 2020 (Fig. 3b).

https://doi.org/10.5194/egusphere-2026-3724
Preprint. Discussion started: 27 July 2026

3.2 Atmospheric water balance at basin scale

Atmospheric moisture fluxes integrated over the Awash Basin by hydrological year (October–September) link regional hydrological changes to large-scale moisture transport. Lakes surface area variations closely follow interannual changes in basin rainfall (Figs. 4a-b) and Awash River discharge (Fig. 4c). Anomalously wet years — notably 1999–2000, 2007, 2010, and 2020, all associated with La Niña conditions — correspond to substantial increases in lake surface area. Notably, although annual rainfall totals during 1985–1995 were not exceptionally low, lake surface area remained considerably smaller than in subsequent years.

In contrast, atmospheric moisture convergence shows a weaker relationship with interannual variations in lake surface area (Fig. 4d), though the magnitude of its variability has increased since around 2000, consistent with the larger interannual fluctuations in the lake system.

Among the remaining water balance components, four of the five actual evapotranspiration datasets (MOD16A2 is excluded owing to its shorter record) indicate that annual totals were considerably higher during 1985–1999 than after 2000 (Fig. 4e), despite relatively modest rainfall in the earlier period. This apparent inconsistency with the concurrent increasing trends in both temperature and potential evaporation (Fig. 4f; Gebrechorkos et al. 2019; Gummadi et al. 2018) is addressed by examining the rainfall–evapotranspiration synchronicity index of Andréassian et al. (2025), which quantifies the fraction of annual rainfall temporally coinciding with peak atmospheric evaporative demand (Fig. 4g). Consistently across all datasets, the index shows high and stable values during 1985–1999, indicating strong seasonal synchronisation between rainfall and potential evaporation, before declining progressively after 2000, suggesting a weakening of this synchronisation.

Figure 5 presents the mean annual cycle of rainfall (CHIRPS v2) and potential evapotranspiration (GLEAM v4.2a) for the periods 1981–1999 and 2000–2024. In both periods, rainfall follows a bimodal regime, with a minor rainy season in MAM and a major one in JAS. Between the two periods, March rainfall decreased from 58 ± 33 to $43 \pm 29\ \mathrm{mm\,month^{-1}}$, while August rainfall increased from 131 ± 30 to $148 \pm 24\ \mathrm{mm\,month^{-1}}$.

Changes in potential evapotranspiration seasonality are even more pronounced. During 1981–1999, peak potential evapotranspiration coincided with the JAS rainfall maximum; after 2000, it shifted to March (GLEAM v4.2a), when rainfall has declined. Other databases (not shown) similarly show increased actual evapotranspiration predominantly in the first half of the year.

Figures 5c and 5d illustrate the JAS rainfall redistribution spatially: significant negative rainfall trends during MAM are concentrated in the central and lower basin, while significant positive trends during JAS occur mainly in the lower basin. These findings are consistent with Getahun et al. (2021), who reported significant decreasing MAM and increasing JAS trends from rain gauge stations, with a breakpoint around 1998. At the regional scale, the MAM decline has been linked to warming in northwestern Eurasia altering large-scale circulation (Hagos et al., 2024), though the recent drying trend in the Horn of Africa appears unusual in a multi-millennial context and may reflect anthropogenic forcing (Tierney et al., 2015).

Together, these results explain the evapotranspiration pattern described above. Before 2000, peak rainfall and peak potential evapotranspiration coincided in JAS, facilitating high actual evapotranspiration despite moderate rainfall totals. After 2000, the

https://doi.org/10.5194/egusphere-2026-3724
Preprint. Discussion started: 27 July 2026

increase in potential evapotranspiration over the first half of the year — when rainfall has declined — reduced the seasonal overlap between water availability and evaporative demand, driving lower actual evapotranspiration and decreased synchronicity index values.

3.3 Teleconnections, large-scale circulation and climate modes driving Awash Basin hydroclimatic variability

The previous sections analyse the hydroclimatic evolution of the Awash Basin from a local perspective. Given that JAS rainfall drives most of the basin's surface water generation (Korecha and Barnston, 2007) and shows significant positive trends over 1981–2024 (Sect. 3.2), this section examines the large-scale atmospheric drivers behind these changes. We first analyse teleconnections between convection over the Awash Basin and large-scale tropical ascent and subsidence, with an emphasis on the role of the main modes of climate variability — including ENSO, the PDO, and the SIOD — in driving the hydroclimatic changes observed over the past 40 years. We then examine the climatology of vertically integrated moisture flux and convergence before investigating long-term trends in moisture transport and their implications for the basin's hydrology.

3.3.1 Teleconnections associated with the Awash Basin convection

Convection over the Awash Basin is characterized using ERA5 500-hPa pressure vertical velocity, a widely used proxy for large-scale convective activity closely linked to the Hadley and Walker circulations (Bony et al., 1997; Sharma et al., 2022; Steiner et al., 2018). Monthly averaging reduces variability from local circulations and short-lived convective events (He et al., 2022).

Figure 6a identifies regions dynamically connected to Awash Basin convection during JAS, where negative correlations indicate that enhanced ascent elsewhere is associated with subsidence — and rainfall deficits — over the basin. The strongest correlations occur over the tropical Pacific, reflecting the well-documented ENSO influence on Kiremt rainfall (Belay et al., 2021; Nicholson, 2017; Tufa and Goshel, 2023), consistent with the results presented in Sect. 2.2.2 and Sect. 3.1. El Niño suppresses Ethiopian convection through two concurrent pathways: enhanced deep convection over the central Pacific weakens the Tropical Easterly Jet (TEJ) and reduces upper-tropospheric divergence over the Horn of Africa (Diro et al., 2011; Gleixner et al., 2017; Rowell, 2001), while the Indian Ocean SST response enhances convection over the Indian Ocean and induces subsidence over parts of Africa (Janicot et al., 2001; Joly and Voldoire, 2009). Consistent with this, Fig. 6b shows significant negative correlations between Lake Abhe surface area and Pacific SSTs during El Niño and positive PDO phases (Lüdecke et al., 2021; Mulualem et al., 2024), as well as negative correlations with western subtropical Indian Ocean SSTs reflecting the influence of the Mascarene High (Camberlin, 1995; Segele et al., 2009a; Terray et al., 2003).

Figure 6a further shows that Awash Basin ascent co-varies positively with Indian monsoon convection (Camberlin, 1997; Vizy and Cook, 2003), convection over the Ethiopian Massif consistent with Atlantic–Congo westerly moisture transport (Segele et al., 2009a; Williams et al., 2012), and ascent over the Arabian Peninsula linked to cyclonic anomalies (Nicholson, 2017; Segele and Lamb, 2005). Subsidence over the South Atlantic High further suggests a regional Walker circulation connecting Atlantic descent to East African ascent. These results provide the dynamical context for the moisture transport and trend analyses presented in the following subsections.

https://doi.org/10.5194/egusphere-2026-3724
Preprint. Discussion started: 27 July 2026

3.3.2 Interannual SST variability and its relationship with the evolution of the Abhe–Afambo–Gemeri lake system

Figure 7 shows detrended annual time series of Lake Abhe surface area alongside the PDO, ENSO (El Niño 4 region), and the SIOD, the latter computed as the SST anomaly difference between the western (55°–58°E, 32°–15°S) and eastern (92°–110°E, 32°–15°S) subtropical Indian Ocean. In agreement with the results of Sect. 3.3, lake surface area correlates negatively with both the El Niño 4 and PDO indices, consistent with the PDO representing long-term ENSO-like Pacific SST variability (Mantua and Hare, 2002), and negatively with the SIOD, suggesting that positive SIOD phases — characterized by anomalous western subtropical Indian Ocean warming — reduce lake extent, possibly through weakening of the Mascarene High and reduced cross-equatorial flow (Segele et al., 2009a, b).

These relationships are reflected in the historical record. Low lake levels during 1985–1995 coincided with predominantly positive PDO and SIOD phases (Behera and Yamagata, 2001; Mantua and Hare, 2002). The post-1997/98 El Niño shift toward negative PDO and SIOD conditions (Lyon et al., 2014) coincided with lake expansion. The sharp lake contraction of 2011–2016 coincided with a PDO shift toward positive conditions around 2014 (Xiao and Ren, 2023), the 2014–2015 and exceptionally strong 2015–2016 El Niño events (Varotsos et al., 2016), and a generally positive SIOD (Yu et al., 2023). Finally, the sharp lake expansions in 2020 and 2024 appear linked to the 2020–2022 La Niña, a negative Indian Ocean Dipole (Cullis and Bogale, 2024), and potentially long-term anthropogenic warming (Green et al., 2025), which may amplify lake-filling precipitation through enhanced thermal gradients associated with strong warming trends over the Arabian Peninsula and the Tibetan Plateau (see Sect.X for a full discussion of these mechanisms).

3.3.3 Regional vertically integrated moisture flux (VIMF), vertically integrated moisture convergence (VIMC) and convection index

Figures 8a–b show the climatological large-scale circulation during boreal summer, with the ITCZ evident as a zonal band of strong moisture convergence and upward motion between 0° and 15°N. Over the Indian Ocean, vertically integrated moisture transport exhibits marked meridional shear — easterly at southern latitudes and westerly north of the equator — consistent with the Indian summer monsoon (Kushwaha et al., 2022). Along the eastern African coast, these easterlies turn northward, forming the Somali Jet (Fig. 8a), which channels moisture toward western India where strong convergence and ascent are observed (Findlater, 1969; Iqbal et al., 2017). Regional topography contributes to accelerating this flow while inducing moisture divergence and suppressed ascent over the eastern Horn of Africa (Chakraborty et al., 2009; Slingo et al., 2005). Over northeastern Africa, southward moisture transport sustains ITCZ rainfall as part of the regional Hadley circulation, with additional moisture advection from the Mediterranean and Red Sea representing a major pathway for Ethiopian Highland precipitation (Viste et al., 2013). Indeed, Kiremt rainfall over Ethiopia receives moisture from three primary sources: (i) the Indian Ocean via the Somali Jet, (ii) the Atlantic Ocean and Congo Basin through the West African monsoon zonal circulation, and (iii) the Mediterranean and Red Seas via the regional meridional overturning circulation (Camberlin, 1995; Viste et al., 2013). The Ethiopian Highlands also play a key dynamical role in generating and maintaining the African Easterly Jet (AEJ; Fig. 8a) through topographically enhanced meridional temperature gradients and latent heat release (Hamilton et al., 2020).

https://doi.org/10.5194/egusphere-2026-3724
Preprint. Discussion started: 27 July 2026

Figures 8c–d highlight significant trends in large-scale atmospheric processes relevant to JAS rainfall over the Awash Basin. Moisture transport associated with the Somali Jet strengthens over the western Arabian Sea (Fig. 8c), consistent with significant positive trends in moisture convergence and convective activity over India (Figs. 8c–d). The regional Hadley circulation shows a meridional redistribution of vertical motion, with significant negative ascent trends between 5°–15°N and 20°–40°E — the climatological ITCZ position — and positive trends farther north between 15°–20°N, suggesting a northward ITCZ displacement (Fig. 8d). Similarly, the AEJ exhibits a dipole structure in moisture transport trends (Fig. 8c): weakening easterlies south of 15°N and strengthening north of it, consistent with reduced ascent over the Sahel and increased ascent over the Sahara, indicating a northward jet displacement (Fig. 8d). The following subsections examine how long-term trend affect the Awash hydro-climatic system.

3.3.4 Trends in the regional Walker and Hadley cells

The teleconnections identified in Sect. 3.3.1 are associated with variations and trends in the Walker and Hadley circulations. The zonal overturning circulation associated with the West African monsoon is examined through a longitude–height cross-section of zonal wind, vertical velocity, and specific humidity (5°S–11°W to 17°N–39°E; red line in Fig. 9a). During boreal summer, low-level westerlies transport moisture from the tropical Atlantic inland, penetrating northward during the early monsoon phase and northeastward during the mature phase (Fig. 9b; Lélé et al., 2015).

Figure 9c shows significant positive trends in low-level specific humidity over the Gulf of Guinea, consistent with ongoing ocean warming and enhanced surface evaporation (Ibebuchi and Obarein, 2025; Wongchuig et al., 2025), alongside strengthening low-level westerlies below 700 hPa. Together, these changes suggest intensified moisture transport into the continent, contributing to positive mid-tropospheric humidity trends east of 15°E. Consistent with Segele et al. (2009b), who linked Horn of Africa rainfall to the Gulf of Guinea–Arabian Peninsula pressure gradient, increasing pressure over the South Atlantic and decreasing pressure over the Arabian Peninsula (Fig. 10b) (the latter consistent with strong warming trends over the region; Fig. 11) strengthen this zonal gradient, potentially enhancing low-level monsoon inflow and rainfall over the Ethiopian Plateau (Fig. 12b), in line with the trans-basin teleconnection mechanism of Kamae et al. (2017).

Figure 9d shows the climatological meridional Hadley cell circulation, with low-level southerly moisture transport peaking near 10°N and the ascending branch near 18°N. Trend analysis (Fig. 9e) reveals a south–north dipole in specific humidity, with positive trends between 18°–28°N accompanied by northward-extending southerly winds and enhanced ascent near 20°N, suggesting a northward shift of the ascending branch. This is corroborated by a gradual northward displacement of the ITCZ within the study region (Fig. 9f), consistent with documented Sahel rainfall recovery since the late twentieth century (Ali and Lebel, 2009; Nicholson, 2005; Odoulami and Akinsanola, 2018) following the severe drought of the 1960s–1980s (Biasutti, 2019). This recovery has been linked to greenhouse gas forcing (Biasutti, 2013; Gaetani et al., 2017), northward AEJ displacement, Tropical Easterly Jet (TEJ) intensification (Nicholson, 2008; Nicholson and Grist, 2001), and the positive phase of the Atlantic Multidecadal Variability since the mid-1990s, which enhances southwesterly flow and moisture convergence over the Sahel (Mohino et al., 2011, 2024; Ting et al., 2011).

https://doi.org/10.5194/egusphere-2026-3724
Preprint. Discussion started: 27 July 2026

3.4 Associated change in the major atmospheric jet affecting East Africa

This section examines the climatology and long-term trends of JAS atmospheric circulation and key dynamical variables associated with the Somali Jet, the Tropical Easterly Jet (TEJ), and the African Easterly Jet (AEJ) at different tropospheric levels (Fig. 10), with the aim of identifying the large-scale mechanisms driving the hydroclimatic changes observed over the Awash Basin.

3.4.1 The Somali Jet

The Asian summer monsoon circulation is driven by an interhemispheric pressure gradient between the Mascarene High (20°S, 60°E) and the low-pressure region over the Arabian Peninsula (20°N, 45°E), visible in Fig. 10a, which forces a northward cross-equatorial flow over the western Arabian Sea (Krishnamurti and Wong, 1979). Interaction with East African orography enhances kinetic energy and modifies the low-level wind structure (Masiwal et al., 2023), while increasing Coriolis deflection transforms the meridional flow into the southwesterly Somali Jet near 10°N, 60°E (Findlater, 1969). This jet drives low-level moisture transport, convective activity, and the onset of the Indian summer monsoon (Boos and Emanuel, 2009; Halpern and Woiceshyn, 2001).

Figure 10b shows that geopotential height has increased over the Mascarene High (non-significantly) and decreased significantly over the Arabian Peninsula — driven by strong near-surface warming (2 m temperature) over the region (Fig. 11) — enhancing the interhemispheric pressure gradient. Consequently, cross-equatorial flow and the Somali Jet show significant intensification trends.

Recent studies report contrasting trends in the Somali Jet, largely reflecting differences in definitions and metrics. Sharma et al. (2025) and Jain et al. (2021) document a post-1998 weakening and northward shift during the early monsoon, reducing moisture transport toward peninsular India and delaying monsoon onset, while a stronger jet in September sustains rainfall and delays withdrawal. Other studies, however, report intensification (Shi et al., 2007, 2016, 2021; Shi and Xiao, 2013), with discrepancies partly attributable to methodological differences in jet characterization.

Here we investigate how the jet influences moisture characteristics at a more local scale. Figure 12a shows climatological JAS precipitation and regional low-level circulation. Rainfall distribution and low-level winds are strongly modulated by topography. Low-level winds from the southern Indian Ocean accelerate through the Kenya–South Sudan topographic gap, forming the Turkana Jet (Kinuthia and Asnani, 1982), before turning northwestward upon encountering the Somali Plateau (∼10°N, 43°E), enhancing orographic lifting and precipitation over the eastern part of the Awash catchment.

Figure 12b presents linear trends in JAS 850-hPa winds and accumulated rainfall. The southerly flow over the western Indian Ocean and the Somali Jet show significant strengthening trends, consistent with the intensification of the interhemispheric pressure gradient discussed above. Along the 43°E cross-section (Figs. 12c–d), strengthening southerly winds between 1000 and 800 hPa enhance moisture transport from the southern Indian Ocean (Fig. 12d), and their interaction with regional topography increases orographic convection near 10°N, raising mid-tropospheric specific humidity (700–500 hPa) and precipitation over

https://doi.org/10.5194/egusphere-2026-3724
Preprint. Discussion started: 27 July 2026

the Somali Plateau (Fig. 12e).These results suggest that the strengthening of the Somali Jet contributes directly to increased precipitation over the elevated southeastern sector of the catchment.

3.4.2 The Tropical Easterly Jet (TEJ)

The Somali Jet plays a well-documented role in modulating the onset and intensity of the Indian summer monsoon, with stronger (weaker) jet conditions associated with wetter (drier) monsoon years (Chen and van Loon, 1987; Halpern and Woiceshyn, 2001; Iqbal et al., 2017). The strengthening trend identified above (Figs. 8c and 10b) is consistent with a significant positive JAS convection trend over India (Fig. 8d). These findings align with Yadav (2025), who linked a west–east rainfall dipole over India to equatorial Indian Ocean warming, which intensifies cross-equatorial flow and moisture convergence over the Arabian Sea.

These findings should be interpreted in the context of pronounced multidecadal monsoon variability, with a declining trend in mean Indian monsoon rainfall during 1950–2002 (Bollasina et al., 2011; Roxy and Chaithra, 2018) followed by a partial recovery since the early 2000s (Bajrang et al., 2023; Jin and Wang, 2017), operating on characteristic timescales of 60–70 years (Sinha et al., 2015).

In the upper troposphere, the TEJ extends from Southeast Asia to West Africa during boreal summer, reaching maximum wind speeds of $\sim$35 m s^{-1} (Fig. 10c), and is primarily driven by thermal gradients associated with Tibetan Plateau heating and latent heat release over the northern Indian Ocean (Krishnamurti, 1971; Nicholson and Klotter, 2021). The TEJ significantly influences Ethiopian rainfall through modulation of upper-level divergence and vertical motion (Diro et al., 2011; Kebede et al., 2025; Segele et al., 2009b). Consistent with the Somali Jet strengthening and enhanced Indian monsoon convection, ERA5 trends show significant TEJ intensification over the equatorial Indian Ocean (Fig. 10d), likely also driven by enhanced upper-tropospheric thermal gradients associated with Tibetan Plateau warming (+0.38 °C decade^{-1}; Fig. 11). Such intensification of the TEJ favors upper-level divergence and convective activity, thereby enhancing summer rainfall at the regional scale, particularly over Sudan and Ethiopia (**?**).

3.4.3 The African Easterly Jet (AEJ)

The AEJ is a mid-tropospheric feature (700–600 hPa,; Fig. 10e) driven by the meridional temperature gradient between the Saharan Heat Low and the cooler, moister Sahel, with additional modulation from the Ethiopian Highlands and Marrah Mountains (Cook, 1999; Hamilton et al., 2020; Parker et al., 2005). Through its control on ITCZ position and the generation of African Easterly Waves, the AEJ shapes the spatial distribution of rainfall and interannual variability across the Sahel (Crétat et al., 2015; Thorncroft and Hoskins, 1994).

ERA5 trends for 1979–2024 reveal latitudinally contrasting zonal wind changes within the AEJ region (Fig. 10f): weakening easterlies between 5°–15°N and strengthening between 15°–25°N, indicating a northward displacement of the jet. This shift is consistent with thermal wind balance: significant 700-hPa, warming, particularly over northeastern Africa (Fig. 10f), has driven a northward migration of the Sahara–Sahel temperature maximum (Fig. 13a), tracked by a corresponding poleward shift in the AEJ latitude index (Fig. 13b), which closely follows the Sahara–Sahel temperature gradient (Fig. 13b).

https://doi.org/10.5194/egusphere-2026-3724
Preprint. Discussion started: 27 July 2026

Northward AEJ excursions are dynamically linked to an expansion of the ascending branch between the AEJ and TEJ, enhancing low-level monsoon flow and moisture convergence over the Sahel (Nicholson and Grist, 2001; Jungandreas et al., 2023). Consistent with this mechanism, CHIRPSv2 trends show significant JAS rainfall increases across the Sahel between 10°–20°N (Figs. 13c–d). This joint northward displacement of the AEJ and the regional overturning circulation, including the ITCZ, may also have implications for rainfall patterns farther east, including the Awash Basin, where shifts in large-scale convergence zones can modulate regional precipitation seasonality.

4 Conclusions

The Awash Basin is a socio-economic and hydrological cornerstone of Ethiopia, hosting the majority of the country's industries, its largest irrigated agriculture area, and critical hydropower and domestic water infrastructure. Yet it remains highly exposed to climate variability and change, with recurrent droughts and floods posing persistent threats to water and food security. The terminal Afambo–Gemeri–Abhe lake system, as a natural integrator of basin-scale hydrological variability, offers a rare opportunity to reconstruct the cumulative response of the basin to climatic forcing across multiple timescales — particularly valuable given the scarcity of long-term in situ observations in the region.

By coupling the GR2M hydrological model with a lake water-balance model, constrained by satellite and in situ observations, this study successfully reconstructs the hydrological history of the lake system over 1985–2024 and bridges the pre-1998 observational gap. This parsimonious framework demonstrates that meaningful hydroclimatic reconstruction is achievable in data-scarce environments, and provides a transferable tool for investigating both past and future lake dynamics using climate simulations from projects such as the Coupled Model Intercomparison Project Phase 6 (CMIP6) and the Paleoclimate Modelling Intercomparison Project Phase 4 (PMIP4).

The reconstructed history reveals two superimposed signals. The first is pronounced interannual to interdecadal variability, modulated by large-scale climate modes — El Niño–Southern Oscillation, the Pacific Decadal Oscillation, and the Subtropical Indian Ocean Dipole — with periods of lake expansion and contraction broadly consistent with the phases of these modes. The second is a sustained multi-decadal expansion, from $\sim$150 km^2 in the 1980s to $\sim$300 km^2 in the early 2000s and $\sim$450 km^2 by 2024, primarily driven by positive July–August–September (JAS) rainfall trends. A complementary finding concerns the seasonal structure of water availability: during 1981–1999, the near-synchrony of peak rainfall and peak potential evapotranspiration in August limited effective water input to the lake, whereas after 2000 a shift in the potential evapotranspiration seasonal maximum toward March — coinciding with increasing JAS rainfall — enhanced net water availability and likely amplified the observed expansion.

These wetter JAS conditions are linked to a coherent set of large-scale atmospheric circulation changes. Warming over the Arabian Peninsula strengthens the interhemispheric pressure gradient and intensifies the Somali Jet, enhancing moisture transport toward Ethiopia — particularly over the southeastern Awash Basin — and promoting forced convection over the Somali Plateau. The intensified Somali Jet also increases moisture transport toward western India, strengthening Indian monsoon convection and, in turn, reinforcing the Tropical Easterly Jet — further supported by warming over the Tibetan Plateau —

https://doi.org/10.5194/egusphere-2026-3724
Preprint. Discussion started: 27 July 2026

which further promotes convection at a regional scale over northeastern Africa. An enhanced pressure gradient between the Atlantic subtropical high and the Arabian Peninsula strengthens the Walker circulation, additionally contributing to increased rainfall over the Ethiopian Highlands through greater Atlantic moisture transport — a process that primarily affects the western Awash Basin. Finally, a northward shift in both the African Easterly Jet and the Intertropical Convergence Zone can modify the seasonality of rainfall across the Awash Basin. These changes are summarized schematically in Figure 14.

Further research is needed to better quantify the relative contributions of these warming patterns to the observed hydrological changes, and to assess the future trajectory of the Afambo–Gemeri–Abhe lake system under ongoing climate change. Extending this hydrological reconstruction beyond the instrumental period would also be valuable, as placing current and projected changes in the perspective of longer-term past variability is essential for distinguishing anthropogenic forced trends from natural climate fluctuations. The modelling framework proposed here is well-suited to this purpose, as it can be driven by paleoclimate simulations and evaluated against independent proxies such as lake sediment records — and, more broadly, against archaeological evidence and historical population dynamics, which in this region are tightly coupled to lake-level and water availability changes. Such multi-archive, multi-timescale approach would both strengthen the robustness of future projections and open new avenues for understanding human–climate–water interactions across the Awash Basin. These projections, combined with improved seasonal forecasts, would directly support water resource management and infrastructure planning — informing decisions on irrigation, hydropower, and flood and drought preparedness in one of Ethiopia's most climatically vulnerable and economically vital regions.

Code availability. The lake model codes are available at https://github.com/JuanPabloSierra/Afambo-Gemeri-Abhe_LakeSystem.git.

Data availability. The CHIRPS v2 dataset is available at https://www.chc.ucsb.edu/data/chirps (last accessed May 2026). The TRMM 3B42 v7 dataset is available at https://search.earthdata.nasa.gov/search?q=TRMM_3B42 (last accessed May 2026). The CMORPH v1.0 dataset is available at https://www.ncei.noaa.gov/products/climate-data-records/precipitation-cmorph (last accessed May 2026). The EartH2Observe reanalysis datasets are available at http://www.earth2observe.eu/?page_id=4542 (last accessed July 2025). The GLEAM v4.2a dataset is available at https://www.gleam.eu/ (last accessed May 2026). The MOD16A2 dataset is available via Google Earth Engine. The CRU TS v4.09 is available at https://crudata.uea.ac.uk/cru/data/hrg/cru_ts_4.09/observation.v4.09/ (last accessed May 2026). The ERA5 dataset is available at https://cds.climate.copernicus.eu/datasets/reanalysis-era5-single-levels-monthly-means?tab=download (last accessed May 2026). The SRTM dataset is available at https://portal.opentopography.org/raster?opentopoID=OTSRTM.082015.4326.1 (last accessed May 2026). The GTOPO dataset is available at https://www.usgs.gov/centers/eros/science/usgs-eros-archive-digital-elevation-global-30-arc-second-elevation-gtopo30 (last accessed May 2026). The PDO index is available at https://www.ncei.noaa.gov/access/monitoring/pdo/ (last accessed February 2026). El Niño SST anomalies are available at NOAA/NCEI: https://www.cpc.ncep.noaa.gov/data/indices/sstoi.indices (last accessed April 2026). The OISST v2.1 dataset is available at https://www.ncei.noaa.gov/products/optimum-interpolation-sst (last accessed May 2026). The GRDC database is available at https://grdc.bafg.de/ (last accessed February 2026). The GSWD dataset is available at https://global-surface-water.appspot.com/download (last accessed May 2026). The Landsat 8–9 imagery is available via Google Earth Engine. The HydroWeb dataset is

https://doi.org/10.5194/egusphere-2026-3724
Preprint. Discussion started: 27 July 2026

available at https://hydroweb.next.theia-land.fr/ (last accessed February 2026). Lake surface areas of the Abhe–Afambo–Gemeri lake system or individual lakes from the lake model will be made available upon acceptance at https://doi.org/10.5281/zenodo.20510341.

Appendix A: Lake model further details and parameter adjustments

The Awash Basin has been extensively modified by hydraulic infrastructure to support irrigated agriculture (Kidane et al., 2014). Seven dams currently operate in the basin (Fig. 1a; Mulligan et al., 2021) and large-scale irrigation development has expanded since the 1960s (Mersha et al., 2018). The Tendaho Dam (completed 2008) supplies water to extensive alluvial plains between Tendaho and Lakes Gemeri and Afambo via irrigation canals with a design discharge capacity of up to 78 $m^3\ s^{-1}$ (Bekele and Alamirew, 2021), equivalent to ∼43% of mean August discharge at Tendaho over 1990–2004 (GRDC observations).

To represent these human impacts in the lake water balance, simulated discharge at Tendaho (Q_0) was partitioned into two branches—Q_1 toward Lake Abhe and Q_2 toward Lakes Gemeri, Afambo, and Bario—after applying a reduction factor p accounting for irrigation abstractions (Fig. 1a). Downstream of Lake Bario, Q_3 merges with Q_1 to yield Q_4, the total inflow to Lake Abhe. The flow partitioning is expressed as:

$$Q_1 = Q_0(1-p)X, \tag{A1}$$

$$Q_2 = Q_0(1-p)Y, \tag{A2}$$

$$Q_3 = Q_2 + S_{\mathrm{NL}}\left(P_{\mathrm{NL}} - E_{\mathrm{NL}}\right), \tag{A3}$$

$$Q_4 = Q_3 + Q_1, \tag{A4}$$

$$X + Y = 1. \tag{A5}$$

where S_{NL} is the surface area of Lakes Gemeri and Afambo, P_{NL} and E_{NL} are precipitation and evaporation over the northern lakes, and X and Y are the fractions of post-abstraction discharge routed to each branch. The effective routing parameters $a = X(1-p)$ and $b = Y(1-p)$ represent the fractions of total discharge routed toward Lake Abhe and the Gemeri–Afambo system, respectively, with p the fraction abstracted for irrigation.

Parameters a, b, and p were estimated dynamically using overlapping 10-year moving windows over 1985–2024. For each window, a and b were varied between 0.1 and 0.5—consistent with the Tendaho irrigation infrastructure capacity of up to ∼43% of rainy-season discharge (Bekele and Alamirew, 2021)—with the optimal parameter set selected by minimizing the mean squared error between modeled and GSWD-derived lake surface areas (Fig. A1a).

The temporal evolution of a, b, and p (Fig. A1b) shows a marked increase in total flow reduction, from $p \approx 0.28$ during 1985–1995 to $p \approx 0.51$ during 2011–2021, before declining to 0.39 in 2014–2024. This trend is consistent with the documented 15% expansion of cultivated areas in the Awash Basin between 1988 and 2018, particularly downstream of the Tendaho Dam (Tadese et al., 2019).

https://doi.org/10.5194/egusphere-2026-3724
Preprint. Discussion started: 27 July 2026

Author contributions. M.R., Pasc. B., and P.B. conceived the project (Conceptualization). P.S.N. developed the lake model and performed the preprocessing of most of the variables needed to run it (Methodology). P.B., C.B., E.C. and N.V. led the development of the lake model (Methodology). C.C.V. and P.S.N. constructed the hypsometric curves for each of the lakes (Methodology). J.P.S. contributed to the finalization and refinement of the lake model (Methodology). Pasc. B. and J.P.S. performed the analyses of atmospheric variables (Formal analysis). J.P.S., P.B., and S.W. performed the analyses of hydrological variables (Formal analysis). J.P.S. was responsible for drafting the article, with contributions from all co-authors (Writing – original draft; Writing – review and editing).

Competing interests. The authors declare that they have no conflict of interest.

Acknowledgements. J.P.S. was supported by a postdoctoral grant from the NILAFAR project, funded by the French National Research Agency (ANR). S.W. was supported by a postdoctoral grant from the French Space Agency (CNES).

References

Abate, Z.: Water resources development in Ethiopia: an evaluation of present experience and future planning concepts, Ithaca Press, Reading, UK, 1994.

Abebe, Y., Alemayehu, T., Abebe, B. A., Alamirew, T., Teckola, B., and Alemayehu, E.: A systematic review of the transformation of Lake Beseka from brine to nearly fresh lake water, Discover Sustainability, 6, https://doi.org/10.1007/s43621-024-00747-9, 2025.

Abtew, W., Melesse, A. M., and Dessalegne, T.: El Niño Southern Oscillation link to the Blue Nile River basin hydrology, Hydrol. Process., 23, 3653–3660, https://doi.org/10.1002/hyp.7367, 2009.

Adam, O., Bischoff, T., and Schneider, T.: Seasonal and interannual variations of the energy flux equator and ITCZ. Part I: zonally averaged ITCZ position, J. Clim., 29, 3219–3230, https://doi.org/10.1175/JCLI-D-15-0512.1, 2016.

Akpoti, K., Velpuri, N., Leh, M., Kagone, S., Mekonnen, K., Owusu, A., Tadesse, M., Prabhath, P. T., Madushanka, L., Perera, T., Parrish, G. E. L., Vinay, N., Sy, S., Bliefernicht, J., Guug, S., Seid, A. H., and Senay, G.: Remote Sensing of Evapotranspiration in Africa: Evaluation of VegET against MODIS16, SSEBop, WaPOR, and GLEAM, with Applications in Drought Monitoring, https://doi.org/10.2139/ssrn.5473213, sSRN working paper, 2025.

Alfieri, L., Libertino, A., Campo, L., Dottori, F., Gabellani, S., Ghizzoni, T., Masoero, A., Rossi, L., Rudari, R., Testa, N., et al.: Impact-based flood forecasting in the Greater Horn of Africa, Nat. Hazards Earth Syst. Sci., 24, 199–224, https://doi.org/10.5194/nhess-24-199-2024, 2024.

Ali, A. and Lebel, T.: The Sahelian standardized rainfall index revisited, International Journal of Climatology, 29, 1705–1714, https://doi.org/10.1002/joc.1832, 2009.

Andréassian, V., Guimaraes, G. M., de Lavenne, A., and Lerat, J.: Time shift between precipitation and evaporation has more impact on annual streamflow variability than the elasticity of potential evaporation, Hydrol. Earth Syst. Sci., 29, 5477–5491, https://doi.org/10.5194/hess-29-5477-2025, 2025.

Awash Basin Authority: Awash River Basin Strategic Plan Main Report, 2017.

Ayenew, T., Kebede, S., and Alemayehu, T.: Environmental isotopes and hydrochemical study applied to surface water and groundwater interaction in the Awash River basin, Hydrol. Process., 22, 1548–1563, https://doi.org/10.1002/hyp.6716, 2008.

Bajrang, C., Attada, R., and Goswami, B. N.: Possible factors for the recent changes in frequency of central Indian summer monsoon precipitation extremes during 2005–2020, npj Climate and Atmospheric Science, 6, 120, https://doi.org/10.1038/s41612-023-00450-y, 2023.

Balsamo, G., Beljaars, A., Scipal, K., Viterbo, P., van den Hurk, B., Hirschi, M., and Betts, A. K.: A revised hydrology for the ECMWF model: verification from field site to terrestrial water storage and impact in the Integrated Forecast System, J. Hydrometeorol., 10, 623–643, https://doi.org/10.1175/2008JHM1068.1, 2009.

Behera, A. and Yamagata, T.: Subtropical SST dipole events in the southern Indian Ocean, Geophysical Research Letters, 28, 327–330, https://doi.org/10.1029/2000GL011451, 2001.

Bekele, E. and Alamirew, T.: Water delivery performance and dependability of irrigation interval in Tendaho Sugar Estate, Ethiopia, Irrigation and Drainage Systems Engineering, 10, 2021.

Belay, A., Demissie, T., Recha, J. W., Oludhe, C., Osano, P. M., Olaka, L. A., Solomon, D., and Berhane, Z.: Analysis of climate variability and trends in southern Ethiopia, Climate, 9, 96, https://doi.org/10.3390/cli9060096, 2021.

Biasutti, M.: Forced Sahel rainfall trends in the CMIP5 archive, Journal of Geophysical Research: Atmospheres, 118, 1613–1623, https://doi.org/10.1002/jgrd.50206, 2013.

Biasutti, M.: Rainfall trends in the African Sahel: Characteristics, processes, and causes, WIREs Climate Change, 10, e591, https://doi.org/10.1002/wcc.591, 2019.

Billi, P., Alemu, Y. T., and Ciampalini, R.: Increased frequency of flash floods in Dire Dawa, Ethiopia: Change in rainfall intensity or human impact?, Nat. Hazards, 76, 1373–1394, https://doi.org/10.1007/s11069-014-1554-0, 2015.

Bollasina, M. A., Ming, Y., and Ramaswamy, V.: Anthropogenic aerosols and the weakening of the South Asian summer monsoon, Science, 334, 502–505, https://doi.org/10.1126/science.1204994, 2011.

Bony, S., Lau, K., and Sud, Y. C.: Sea surface temperature and large-scale circulation influences on tropical greenhouse effect and cloud radiative forcing, J. Clim., 10, 2055–2077, https://doi.org/10.1175/1520-0442(1997)010<2055:SSTALS>2.0.CO;2, 1997.

Boos, W. R. and Emanuel, K. A.: Annual intensification of the Somali jet in a quasi-equilibrium framework: Observational composites, Quarterly Journal of the Royal Meteorological Society, 135, 319–335, https://doi.org/10.1002/qj.388, 2009.

Bouchez, C., Goncalves, J., Deschamps, P., Vallet-Coulomb, C., Hamelin, B., Doumnang, J.-C., and Sylvestre, F.: Hydrological, chemical, and isotopic budgets of Lake Chad: a quantitative assessment of evaporation, transpiration and infiltration fluxes, Hydrology and Earth System Sciences, 20, 1599–1619, https://doi.org/10.5194/hess-20-1599-2016, 2016.

Camberlin, P.: June–September rainfall in north-eastern Africa and atmospheric signals over the tropics: a zonal perspective, Int. J. Climatol., 15, 773–783, https://doi.org/10.1002/joc.3370150705, 1995.

Camberlin, P.: Rainfall Anomalies in the Source Region of the Nile and Their Connection with the Indian Summer Monsoon, Journal of Climate, 10, 1380–1392, https://doi.org/10.1175/1520-0442(1997)010<1380:RAITSR>2.0.CO;2, 1997.

Chakraborty, A., Nanjundiah, R. S., and Srinivasan, J.: Impact of African orography and the Indian summer monsoon on the low-level Somali jet, Int. J. Climatol., 29, 983–992, https://doi.org/10.1002/joc.1720, 2009.

Chen, T. and van Loon, H.: Interannual variation of the tropical easterly jet, Monthly Weather Review, 115, 1739–1759, https://doi.org/10.1175/1520-0493(1987)115<1739:IVOTTE>2.0.CO;2, 1987.

Conway, D., Dalin, C., Landman, W. A., and Osborn, T. J.: Hydropower plans in eastern and southern Africa increase risk of concurrent climate-related electricity supply disruption, Nat. Energy, 2, 946–953, https://doi.org/10.1038/s41560-017-0037-4, 2017.

Cook, K. H.: Generation of the African easterly jet and its role in determining West African precipitation, Journal of Climate, 12, 1165–1184, https://doi.org/10.1175/1520-0442(1999)012<1165:GOTAEJ>2.0.CO;2, 1999.

Crétat, J., Vizy, E. K., and Cook, K. H.: The relationship between African easterly waves and daily rainfall over West Africa: observations and regional climate simulations, Climate Dynamics, 44, 385–404, https://doi.org/10.1007/s00382-014-2120-x, 2015.

Cullis, A. and Bogale, S.: Aligned climate drivers and potential impacts on food security in Ethiopia: Supporting pastoralism and agriculture in recurrent and protracted crises, 2024.

Degefu, D. M., He, W., and Zhao, J. H.: Hydropower for sustainable water and energy development in Ethiopia, Sustain. Water Resour. Manag., 1, 305–314, https://doi.org/10.1007/s40899-015-0029-0, 2015.

Degefu, M. A., Rowell, D. P., and Bewket, W.: Teleconnections between Ethiopian rainfall variability and global SSTs: observations and methods for model evaluation, Meteorol. Atmos. Phys., 129, 173–186, https://doi.org/10.1007/s00703-016-0466-9, 2017.

Di Nunno, F., Yildiz, M. B., Afework, Y. G., de Marinis, G., and Granata, F.: Mapping drought evolution in Ethiopia: trends, clustering, and Bayesian estimation of abrupt changes, Nat. Hazards, 121, 3775–3803, https://doi.org/10.1007/s11069-024-06935-0, 2025.

https://doi.org/10.5194/egusphere-2026-3724
Preprint. Discussion started: 27 July 2026

Dinku, T., Funk, C., Peterson, P., Maidment, R., Tadesse, T., Gadain, H., and Ceccato, P.: Validation of the CHIRPS satellite rainfall estimates over eastern Africa, Q. J. R. Meteorol. Soc., 144, 292–312, https://doi.org/10.1002/qj.3244, 2018.

Diro, G. T., Grimes, D. I. F., and Black, E.: Teleconnections between Ethiopian summer rainfall and sea surface temperature: part I—observation and modelling, Climate Dynamics, 37, 103–119, https://doi.org/10.1007/s00382-010-0837-8, 2011.

Edossa, D. C., Babel, M. S., and Das Gupta, A.: Drought analysis in the Awash river basin, Ethiopia, Water Resour. Manag., 24, 1441–1460, https://doi.org/10.1007/s11269-009-9508-0, 2010.

FAO: Drought in the Horn of Africa: Progress report on the rapid response and mitigation plan to avert a humanitarian catastrophe (January–December 2022), Tech. rep., Food and Agriculture Organization of the United Nations, Rome, https://doi.org/10.4060/cc4218en, 2023.

Farr, T. G. et al.: The Shuttle Radar Topography Mission, Rev. Geophys., 45, RG2004, https://doi.org/10.1029/2005RG000183, 2007.

FEWS NET: Ethiopia Food Security Outlook: June 2022 to January 2023, 2023.

Findlater, J.: Interhemispheric transport of air in the lower troposphere over the western Indian Ocean, Q. J. R. Meteorol. Soc., 95, 400–403, https://doi.org/10.1002/qj.49709540412, 1969.

Finney, D. L., Marsham, J. H., Walker, D. P., Birch, C. E., Woodhams, B. J., Jackson, L. S., and Hardy, S.: The effect of westerlies on East African rainfall and the associated role of tropical cyclones and the Madden–Julian Oscillation, Q. J. R. Meteorol. Soc., 146, 647–664, https://doi.org/10.1002/qj.3698, 2020.

Funk, C., Dettinger, M. D., Michaelsen, J. C., Verdin, J. P., Brown, M. E., Barlow, M., and Hoell, A.: Warming of the Indian Ocean threatens eastern and southern African food security but could be mitigated by agricultural development, Proc. Natl. Acad. Sci. U.S.A., 105, 11 081–11 086, https://doi.org/10.1073/pnas.0708196105, 2008.

Funk, C., Peterson, P., Landsfeld, M., Pedreros, D., Verdin, J., Shukla, S., Husak, G., Rowland, J., Harrison, L., Hoell, A., et al.: The climate hazards infrared precipitation with stations–a new environmental record for monitoring extremes, Sci. Data, 2, 150 066, https://doi.org/10.1038/sdata.2015.66, 2015.

Gaetani, M., Flamant, C., Bastin, S., et al.: West African monsoon dynamics and precipitation: the competition between global SST warming and CO2 increase in CMIP5 idealized simulations, Climate Dynamics, 48, 1353–1373, https://doi.org/10.1007/s00382-016-3146-z, 2017.

Gebrechorkos, S. H., Hülsmann, S., and Bernhofer, C.: Changes in temperature and precipitation extremes in Ethiopia, Kenya, and Tanzania, Int. J. Climatol., 39, 18–30, https://doi.org/10.1002/joc.5777, 2019.

Gemechu, T. M., Zhang, H., Sun, J., and Chen, B.: Assessing the Impact of Multi-Decadal Land Use Change on Agricultural Water–Energy Dynamics in the Awash Basin, Ethiopia: Insights from Remote Sensing and Hydrological Modeling, Agronomy, 15, 2804, https://doi.org/10.3390/agronomy15122804, 2025.

Gesch, D. B., Verdin, K. L., and Greenlee, S. K.: New land surface digital elevation model covers the Earth, Eos Trans. AGU, 80, 69–70, https://doi.org/10.1029/99EO00050, 1999.

Getahun, Y. S., Li, M., and Pun, I.: Trend and change-point detection analyses of rainfall and temperature over the Awash River basin of Ethiopia, Heliyon, 7, 2021.

Gleixner, S., Keenlyside, N., Viste, E., et al.: The El Niño effect on Ethiopian summer rainfall, Climate Dynamics, 49, 1865–1883, https://doi.org/10.1007/s00382-016-3421-z, 2017.

Green, A. C., Fowler, H. J., Blenkinsop, S., et al.: Precipitation extremes in 2024, Nat. Rev. Earth Environ., 6, 243–245, https://doi.org/10.1038/s43017-025-00666-x, 2025.

Gummadi, S., Rao, K. P. C., Seid, J., et al.: Spatio-temporal variability and trends of precipitation and extreme rainfall events in Ethiopia (1980–2010), Theor. Appl. Climatol., 134, 1315–1328, https://doi.org/10.1007/s00704-017-2340-1, 2018.

https://doi.org/10.5194/egusphere-2026-3724
Preprint. Discussion started: 27 July 2026

Hagos, S., Chang, C.-C. J., Ma, P.-L., Lubis, S. W., Balaguru, K., Shi, P., et al.: Synchronization of the recent decline of East African long rains and northwestern Eurasian warming, J. Geophys. Res. Atmos., 129, e2024JD041 033, https://doi.org/10.1029/2024JD041033, 2024.

Haile, G. G., Tang, Q., Hosseini-Moghari, S. M., Liu, X., Gebremicael, T. G., Leng, G., Kebede, A., Xu, X., and Yun, X.: Projected impacts of climate change on drought patterns over East Africa, Earths Future, 8, e2020EF001 502, https://doi.org/10.1029/2020EF001502, 2020.

Halpern, D. and Woiceshyn, P. M.: Somali jet in the Arabian Sea, El Niño, and India rainfall, Journal of Climate, 14, 434–441, https://doi.org/10.1175/1520-0442(2001)014<0434:SJITAS>2.0.CO;2, 2001.

Hamilton, H. L., Núñez Ocasio, K. M., Evans, J. L., Young, G. S., and Fuentes, J. D.: Topographic influence on the African Easterly Jet and African Easterly Wave energetics, J. Geophys. Res. Atmos., 125, e2019JD032 138, https://doi.org/10.1029/2019JD032138, 2020.

Harris, I., Osborn, T. J., Jones, P., et al.: Version 4 of the CRU TS monthly high-resolution gridded multivariate climate dataset, Sci. Data, 7, 109, https://doi.org/10.1038/s41597-020-0453-3, 2020.

Hastenrath, S.: Variations of East African climate during the past two centuries, Clim. Change, 50, 209–217, https://doi.org/10.1023/A:1010678111442, 2001.

He, J., Brogniez, H., and Picon, L.: Evaluation of tropical water vapour from CMIP6 global climate models using ESA CCI datasets, Atmos. Chem. Phys., 22, 12 591–12 606, https://doi.org/10.5194/acp-22-12591-2022, 2022.

Hersbach, H., Bell, B., Berrisford, P., et al.: The ERA5 global reanalysis, Q. J. R. Meteorol. Soc., 146, 1999–2049, https://doi.org/10.1002/qj.3803, 2020.

Hirpa, F. A., Alfieri, L., Lees, T., Peng, J., Dyer, E., and Dadson, S. J.: Streamflow response to climate change in the Greater Horn of Africa, Clim. Change, 156, 341–363, https://doi.org/10.1007/s10584-019-02547-x, 2019.

Huang, B., Liu, C., Banzon, V., Freeman, E., Graham, G., Hankins, B., Smith, T., and Zhang, H.: Improvements of the Daily Optimum Interpolation Sea Surface Temperature (DOISST) Version 2.1, J. Clim., 34, 2923–2939, https://doi.org/10.1175/JCLI-D-20-0166.1, 2021.

Huffman, G. J., Bolvin, D. T., Nelkin, E. J., Wolff, D. B., Adler, R. F., Gu, G., Hong, Y., Bowman, K. P., and Stocker, E. F.: The TRMM Multisatellite Precipitation Analysis (TMPA): Quasi-Global, Multiyear, Combined-Sensor Precipitation Estimates at Fine Scales, J. Hydrometeorol., 8, 38–55, https://doi.org/10.1175/JHM560.1, 2007.

Ibebuchi, C. C. and Obarein, O. A.: High and low-frequency climate modes associated with sub-seasonal sea surface temperature variability in the Gulf of Guinea, Theoretical and Applied Climatology, 156, 157, https://doi.org/10.1007/s00704-025-05389-z, 2025.

Iqbal, W., Syed, F. S., Sajjad, H., Nikulin, G., Kjellström, E., and Hannachi, A.: Mean climate and representation of jet streams in CORDEX South Asia simulations using RCA4, Theor. Appl. Climatol., 129, 1–19, 2017.

Jain, S., Mishra, S. K., Anand, A., et al.: Historical and projected low-frequency variability in the Somali jet and Indian summer monsoon, Climate Dynamics, 56, 749–765, https://doi.org/10.1007/s00382-020-05492-z, 2021.

Janicot, S., Trzaska, S., and Poccard, I.: Summer Sahel-ENSO teleconnection and decadal time scale SST variations, Climate Dynamics, 18, 303–320, https://doi.org/10.1007/s003820100172, 2001.

Jin, Q. and Wang, C.: A revival of Indian summer monsoon rainfall since 2002, Nature Climate Change, 7, 587–594, https://doi.org/10.1038/nclimate3348, 2017.

Joly, M. and Voldoire, A.: Influence of ENSO on the West African Monsoon: Temporal Aspects and Atmospheric Processes, Journal of Climate, 22, 3193–3210, https://doi.org/10.1175/2008JCLI2450.1, 2009.

Joyce, R. J., Janowiak, J. E., Arkin, P. A., and Xie, P.: CMORPH: A method that produces global precipitation estimates from passive microwave and infrared data at high spatial and temporal resolution, J. Hydrometeor., 5, 487–503, https://doi.org/10.1175/1525-7541(2004)005<0487:CAMTPG>2.0.CO;2, 2004.

https://doi.org/10.5194/egusphere-2026-3724
Preprint. Discussion started: 27 July 2026

Jungandreas, L., Hohenegger, C., and Claussen, M.: How does the explicit treatment of convection alter the precipitation–soil hydrology interaction in the mid-Holocene African humid period?, Climate of the Past, 19, 637–664, https://doi.org/10.5194/cp-19-637-2023, 2023.

Kamae, Y., Li, X., Xie, S. P., et al.: Atlantic effects on recent decadal trends in global monsoon, Climate Dynamics, 49, 3443–3455, https://doi.org/10.1007/s00382-017-3522-3, 2017.

Kebede, A., Kenea, S. T., Labzovskii, L. D., et al.: The role of the tropical easterly jet on improving the predictability of summer rainfall variability over the Upper Blue Nile Basin in Ethiopia, Theoretical and Applied Climatology, 156, 393, https://doi.org/10.1007/s00704-025-05630-9, 2025.

Kebede, S., Charles, K., Godfrey, S., MacDonald, A., and Taylor, R. G.: Regional-scale interactions between groundwater and surface water under changing aridity: evidence from the River Awash Basin, Ethiopia, Hydrol. Sci. J., 66, 450–463, https://doi.org/10.1080/02626667.2021.1874613, 2021.

Kidane, D., Teketay, D., and Mekonnen, A.: Contributions of Tendaho Irrigation Project to the improvement of livelihoods of agropastoralists in the lower Awash Basin, Northeastern Ethiopia, Ethiopian e-Journal for Research and Innovation Foresight (Ee-JRIF), 6, 2014.

Kinuthia, J. H. and Asnani, G. C.: A newly found jet in North Kenya (Turkana Channel), Monthly Weather Review, 110, 1722–1728, https://doi.org/10.1175/1520-0493(1982)110<1722:ANFJIN>2.0.CO;2, 1982.

Knijff, J., Younis, J., and de Roo, A.: LISFLOOD: A GIS-based distributed model for river basin scale water balance and flood simulation, Int. J. Geogr. Inf. Sci., 24, 189–212, https://doi.org/10.1080/13658810802549154, 2010.

Kobe, F. T.: Understanding climate change in Ethiopia: impacts and solutions, Int. J. Big Data Min. Glob. Warm., 5, 2330 001, https://doi.org/10.1142/S2630534823300014, 2023.

Korecha, D. and Barnston, A. G.: Predictability of June–September rainfall in Ethiopia, Mon. Weather Rev., 135, 628–650, https://doi.org/10.1175/MWR3304.1, 2007.

Krishnamurti, T. N.: Observational study of the tropical upper tropospheric motion field during the Northern Hemisphere summer, Journal of Applied Meteorology and Climatology, 10, 1066–1096, https://doi.org/10.1175/1520-0450(1971)010<1066:OSOTTU>2.0.CO;2, 1971.

Krishnamurti, T. N. and Wong, V.: A planetary boundary-layer model for the Somali jet, Journal of the Atmospheric Sciences, 36, 1895–1907, https://doi.org/10.1175/1520-0469(1979)036<1895:APBLMF>2.0.CO;2, 1979.

Krivoguz, D., Chernyi, S., Zhilenkov, A., Sokolova, S., Moiseev, I., Khalutin, A., and Pisarev, T.: The impact of climate change and regime shifts on the lake dynamics of the Ethiopian Rift Valley, Discover Applied Sciences, 7, 277, https://doi.org/10.1007/s42452-025-06743-6, 2025.

Kushwaha, V. K., Kumar, S. P., Feba, F., et al.: Findlater jet induced summer monsoon memory in the Arabian Sea, Sci. Rep., 12, 13 037, https://doi.org/10.1038/s41598-022-17025-1, 2022.

Le, J. A., El-Askary, H. M., Allali, M., et al.: Characterizing El Niño-Southern Oscillation effects on the Blue Nile yield and the Nile River Basin precipitation using empirical mode decomposition, Earth Syst. Environ., 4, 699–711, https://doi.org/10.1007/s41748-020-00192-4, 2020.

Lehner, B. and Grill, G.: Global river hydrography and network routing: baseline data and new approaches to study the world's large river systems, Hydrological Processes, 27, 2171–2186, https://doi.org/10.1002/hyp.9740, 2021.

Liao, M., Wang, W., and Liu, J.: Spatiotemporal characteristics of lake water level, surface area, and storage changes in Central East Africa from 2018 to 2024, J. Hydrol.: Reg. Stud., 62, 102 842, https://doi.org/10.1016/j.ejrh.2025.102842, 2025.

Lyon, B. and DeWitt, D. G.: A recent and abrupt decline in the East African long rains, Geophys. Res. Lett., 39, L02 702, https://doi.org/10.1029/2011GL050337, 2012.

Lyon, B., Barnston, A. G., and DeWitt, D. G.: Tropical Pacific forcing of a 1998–1999 climate shift: Observational analysis and climate model results for the boreal spring season, Clim. Dyn., 43, 893–909, https://doi.org/10.1007/s00382-013-1891-9, 2014.

Lélé, M. I., Leslie, L. M., and Lamb, P. J.: Analysis of Low-Level Atmospheric Moisture Transport Associated with the West African Monsoon, Journal of Climate, 28, 4414–4430, https://doi.org/10.1175/JCLI-D-14-00746.1, 2015.

Lüdecke, H., Müller-Plath, G., Wallace, M. G., and Lünin, S.: Decadal and multidecadal natural variability of African rainfall, Journal of Hydrology: Regional Studies, 34, 100 795, https://doi.org/10.1016/j.ejrh.2021.100795, 2021.

Mabumbo, D., Nohayi, N., Sanchez Ramirez, J. C., Dessalegn, M., and Ruckstuhl, S.: Navigating climate resilience in fragile settings: a retrospective analysis of the 2023 flood impacts, early warning, and response in Ethiopia's Somali Region, international Water Management Institute (IWMI) report, 2024.

Malede, D. A., Andualem, T. G., Yibeltal, M., Alamirew, T., Kassie, A. E., Demeke, G. G., and Mekonnen, Y. G.: Climate change impacts on hydroclimatic variables over Awash basin, Ethiopia: a systematic review, Discover Applied Sciences, 6, 27, https://doi.org/10.1007/s42452-024-05640-8, 2024.

Mamo, S., Berhanu, B., and Melesse, A. M.: Historical flood events and hydrological extremes in Ethiopia, in: Extreme hydrology and climate variability, pp. 379–384, Elsevier, https://doi.org/10.1016/B978-0-12-815998-9.00029-4, 2019.

Mantua, N. J. and Hare, S. R.: The Pacific Decadal Oscillation, Journal of Oceanography, 58, 35–44, https://doi.org/10.1023/A:1015820616384, 2002.

Masiwal, R., Dixit, V., and Seshadri, A. K.: Explaining dynamics and rapid onset of the Somali jet through its kinetic energy budget, Journal of the Atmospheric Sciences, 80, 833–847, https://doi.org/10.1175/JAS-D-22-0160.1, 2023.

Maslin, M. A., Brierley, C. M., Milner, A. M., Shultz, S., Trauth, M. H., and Wilson, K. E.: East African climate pulses and early human evolution, Quat. Sci. Rev., 101, 1–17, https://doi.org/10.1016/j.quascirev.2014.06.012, 2014.

Mekonnen, Y. A. and Gokcekus, H.: Causes and effects of drought in northern parts of Ethiopia, Civil Environ. Res., 12, https://doi.org/10.7176/CER/12-3-04, 2020.

Melkamu, T., Bagyaraj, M., Adimaw, M., Ngusie, A., and Karuppannan, S.: Detecting and mapping flood inundation areas in Fogera-Dera Floodplain, Ethiopia during an extreme wet season using Sentinel-1 data, Phys. Chem. Earth, 121, 103 189, https://doi.org/10.1016/j.pce.2022.103189, 2022.

Mersha, A. N., Masih, I., De Fraiture, C., Wenninger, J., and Alamirew, T.: Evaluating the impacts of IWRM policy actions on demand satisfaction and downstream water availability in the Upper Awash Basin, Ethiopia, Water, 10, 892, https://doi.org/10.3390/w10070892, 2018.

Messager, M., Lehner, B., Grill, G., et al.: Estimating the volume and age of water stored in global lakes using a geo-statistical approach, Nat. Commun., 7, 13 603, https://doi.org/10.1038/ncomms13603, 2016.

Miralles, D. G., Bonte, O., Koppa, A., et al.: GLEAM4: global land evaporation and soil moisture dataset at 0.1° resolution from 1980 to near present, Sci. Data, 12, 416, https://doi.org/10.1038/s41597-025-04610-y, 2025.

Mohino, E., Janicot, S., and Bader, J.: Sahel rainfall and decadal to multi-decadal sea surface temperature variability, Climate Dynamics, 37, 419–440, https://doi.org/10.1007/s00382-010-0867-2, 2011.

Mohino, E., Monerie, P.-A., Mignot, J., Diakhaté, M., Donat, M., Roberts, C. D., and Doblas-Reyes, F.: Impact of Atlantic multidecadal variability on rainfall intensity distribution and timing of the West African monsoon, Earth System Dynamics, 15, 15–40, https://doi.org/10.5194/esd-15-15-2024, 2024.

Mologni, C., Revel, M., Chaumillon, E., Malet, E., Coulombier, T., Sabatier, P., Brigode, P., Hervé, G., Develle, A. L., Schenini, L., et al.: 50-year seasonal variability in East African droughts and floods recorded in central Afar lake sediments (Ethiopia) and their connections with the El Niño–Southern Oscillation, Clim. Past, 20, 1837–1860, https://doi.org/10.5194/cp-20-1837-2024, 2024.

Mouelhi, S., Michel, C., Perrin, C., and Andréassian, V.: Stepwise development of a two-parameter monthly water balance model, J. Hydrol., 318, 200–214, https://doi.org/10.1016/j.jhydrol.2005.06.014, 2006.

Mullen, C., Penny, G., and Muller, M. F.: A simple cloud-filling approach for remote sensing water cover assessments, Hydrol. Earth Syst. Sci., 25, 2373–2386, https://doi.org/10.5194/hess-25-2373-2021, 2021.

Muller, S., Cáceres, H., Eisner, D., Flörke, S., Herbert, M., Niemann, C., Peiris, C., Popat, T. A., Portmann, E., Reinecke, F. T., Schumacher, R., Shadkam, M., Telteu, S., Trautmann, C. E., and Döll, P.: The global water resources and use model WaterGAP v2.2d: model description and evaluation, Geosci. Model Dev., 14, 1037–1079, https://doi.org/10.5194/gmd-14-1037-2021, 2021.

Mulligan, M., Lehner, B., Zarfl, C., et al.: Global Dam Watch: curated data and tools for management and decision making, Environmental Research: Infrastructure and Sustainability, 1, 033 003, https://doi.org/10.1088/2634-4505/ac333a, 2021.

Mulualem, G. M., Raju, U. J. P., Stojanovic, M., and Sorí, R.: The phenomenon of drought in Ethiopia: Historical evolution and climatic forcing, Hydrol. Res., 55, 595–612, https://doi.org/10.2166/nh.2024.192, 2024.

Nicholson, S.: On the question of the “recovery” of the rains in the West African Sahel, Journal of Arid Environments, 63, 615–641, https://doi.org/10.1016/j.jaridenv.2005.03.004, 2005.

Nicholson, S. and Klotter, D.: The tropical easterly jet over Africa, its representation in six reanalysis products, and its association with Sahel rainfall, International Journal of Climatology, 41, 328–347, https://doi.org/10.1002/joc.6623, 2021.

Nicholson, S. E.: The intensity, location and structure of the tropical rainbelt over west Africa as factors in interannual variability, International Journal of Climatology, 28, 1775–1785, https://doi.org/10.1002/joc.1507, 2008.

Nicholson, S. E.: Climate and climatic variability of rainfall over eastern Africa, Rev. Geophys., 55, 590–635, https://doi.org/10.1002/2016RG000544, 2017.

Nicholson, S. E. and Grist, J. P.: A conceptual model for understanding rainfall variability in the West African Sahel on interannual and interdecadal timescales, International Journal of Climatology, 21, 1733–1757, https://doi.org/10.1002/joc.648, 2001.

Nigusse, A. G. and Adhanom, O. G.: Flood hazard and flood risk vulnerability mapping using geo-spatial and MCDA around Adigrat, Tigray region, Northern Ethiopia, Momona Ethiop. J. Sci., 11, 90–107, https://doi.org/10.4314/mejs.v11i1.6, 2019.

Odoulami, R. C. and Akinsanola, A. A.: Recent assessment of West African summer monsoon daily rainfall trends, Weather, 73, 283–287, https://doi.org/10.1002/wea.2965, 2018.

Ogato, G. S., Bantider, A., Abebe, K., and Geneletti, D.: Geographic information system (GIS)-based multicriteria analysis of flooding hazard and risk in Ambo Town and its watershed, West Shoa Zone, Oromia Regional State, Ethiopia, J. Hydrol.: Reg. Stud., 27, 100 659, https://doi.org/10.1016/j.ejrh.2019.100659, 2020.

Okech, E. O., Kitaka, N., Omondi, S., and Verschuren, D.: Water level fluctuations in Lake Baringo, Kenya, during the 19th and 20th centuries: Evidence from lake sediments, Afr. J. Aquat. Sci., 44, 25–33, https://doi.org/10.2989/16085914.2019.1583087, 2019.

Palmer, P. I., Wainwright, C. M., Dong, B., Maidment, R. I., Wheeler, K. G., Gedney, N., Hickman, J. E., Madani, N., Folwell, S. S., Abdo, G., et al.: Drivers and impacts of Eastern African rainfall variability, Nat. Rev. Earth Environ., 4, 254–270, https://doi.org/10.1038/s43017-023-00397-x, 2023.

Parker, D. J., Thorncroft, C. D., Burton, R. R., and Diongue-Niang, A.: Analysis of the African easterly jet using aircraft observations from the JET2000 experiment, Quarterly Journal of the Royal Meteorological Society, 131, 1461–1482, https://doi.org/10.1256/qj.03.189, 2005.

Pekel, J. F., Cottam, A., Gorelick, N., et al.: High-resolution mapping of global surface water and its long-term changes, Nature, 540, 418–422, https://doi.org/10.1038/nature20584, 2016.

Philip, S., Kew, S. F., Jan van Oldenborgh, G., Otto, F., O'Keefe, S., Haustein, K., King, A., Zegeye, A., Eshetu, Z., Hailemariam, K., et al.: Attribution analysis of the Ethiopian drought of 2015, J. Clim., 31, 2465–2486, https://doi.org/10.1175/JCLI-D-17-0274.1, 2018.

Pörtner, H.-O., Roberts, D. C., Tignor, M., Poloczanska, E. S., Mintenbeck, K., Alegría, A., Craig, M., Langsdorf, S., Löschke, S., Möller, V., Okem, A., and Rama, B., eds.: Climate Change 2022: Impacts, Adaptation and Vulnerability. Contribution of Working Group II to the Sixth Assessment Report of the Intergovernmental Panel on Climate Change, Cambridge University Press, Cambridge, UK and New York, NY, USA, https://doi.org/10.1017/9781009325844, 2022.

Qu, C., Hao, X., and Qu, J. J.: Monitoring extreme agricultural drought over the Horn of Africa (HOA) using remote sensing measurements, Remote Sens., 11, 902, https://doi.org/10.3390/rs11080902, 2019.

Richardson, K., Calow, R., Pichon, F., New, S., and Osborne, R.: Climate risk report for the East Africa region, met Office, ODI, FCDO (UK), 2022.

Rowell, D. P.: Teleconnections between the tropical Pacific and the Sahel, Quarterly Journal of the Royal Meteorological Society, 127, 1683–1706, https://doi.org/10.1002/qj.49712757512, 2001.

Roxy, M. K. and Chaithra, S. T.: Impacts of climate change on the Indian summer monsoon, Tech. rep., Ministry of Environment, Forest and Climate Change, Government of India, 2018.

Running, S., Mu, Q., and Zhao, M.: MOD16A2 MODIS/Terra Net Evapotranspiration 8-Day L4 Global 500m SIN Grid V006, https://doi.org/10.5067/MODIS/MOD16A2.006, nASA LP DAAC, 2017.

Schaebitz, F., Asrat, A., Lamb, H. F., Cohen, A. S., Foerster, V., Duesing, W., Kaboth-Bahr, S., Opitz, S., Viehberg, F. A., Vogelsang, R., et al.: Hydroclimate changes in eastern Africa over the past 200,000 years may have influenced early human dispersal, Commun. Earth Environ., 2, 123, https://doi.org/10.1038/s43247-021-00195-7, 2021.

Segele, Z. and Lamb, P.: Characterization and variability of Kiremt rainy season over Ethiopia, Meteorology and Atmospheric Physics, 89, 153–180, https://doi.org/10.1007/s00703-005-0127-x, 2005.

Segele, Z. T., Lamb, P. J., and Leslie, L. M.: Large-scale atmospheric circulation and global sea surface temperature associations with Horn of Africa June–September rainfall, International Journal of Climatology, 29, 1075–1100, https://doi.org/10.1002/joc.1751, 2009a.

Segele, Z. T., Lamb, P. J., and Leslie, L. M.: Seasonal-to-Interannual Variability of Ethiopia/Horn of Africa Monsoon. Part I: Associations of Wavelet-Filtered Large-Scale Atmospheric Circulation and Global Sea Surface Temperature, Journal of Climate, 22, 3396–3421, https://doi.org/10.1175/2008JCLI2859.1, 2009b.

Sharma, S., Ha, K. J., Cai, W., et al.: Local meridional circulation changes contribute to a projected slowdown of the Indian Ocean Walker circulation, npj Clim. Atmos. Sci., 5, 15, https://doi.org/10.1038/s41612-022-00242-w, 2022.

Sharma, V., Amarjeet, Singh, G. P., et al.: Variabilities in onset and withdrawal characteristics of Indian summer monsoon after 1998 climate shift: dynamical role of Somali jet, Theoretical and Applied Climatology, 156, 557, https://doi.org/10.1007/s00704-025-05760-0, 2025.

Shi, N., Feng, G., Gu, J., Gu, D., and Yu, J.: Climatological variation of global cross-equatorial flows for the period 1948–2004, Journal of Tropical Meteorology, 13, 201–204, 2007.

Shi, W. and Xiao, Z.: Variation of the cross-equatorial moisture transport in Somali and its impact on China early summer rainfall in nearly 60 years, Meteorological Monthly, 39, https://doi.org/10.7519/j.issn.1000-0526.2013.01.005, 2013.

Shi, W., Xiao, Z., and Xue, J.: Teleconnected influence of the boreal winter Antarctic Oscillation on the Somali jet: bridging role of sea surface temperature in southern high and middle latitudes, Advances in Atmospheric Sciences, 33, 47–57, https://doi.org/10.1007/s00376-015-5094-7, 2016.

Shi, W., Wang, Q., Xiao, Z., Cheng, W., and Duan, W.: Modulation of Atlantic Multidecadal Oscillation on the interdecadal variation of South Asian High and Somali jet in summer, Frontiers in Earth Science, 9, 772 202, https://doi.org/10.3389/feart.2021.772202, 2021.

Singh, R., Worku, M., Bogale, S., Cullis, A., Adem, A., Irwin, B., Lim, S., Bosi, L., and Venton, C. C.: Reality of resilience: Perspectives of the 2015–16 drought in Ethiopia, 2016.

Sinha, A., Kathayat, G., Cheng, H., et al.: Trends and oscillations in the Indian summer monsoon rainfall over the last two millennia, Nature Communications, 6, 6309, https://doi.org/10.1038/ncomms7309, 2015.

Slingo, J., Spencer, H., Hoskins, B., Berrisford, P., and Black, E.: The meteorology of the western Indian Ocean and the influence of the East African Highlands, Philos. Trans. R. Soc. A, 363, 25–42, https://doi.org/10.1098/rsta.2004.1473, 2005.

Steiner, A. K., Lackner, B. C., and Ringer, M. A.: Tropical convection regimes in climate models: evaluation with satellite observations, Atmos. Chem. Phys., 18, 4657–4672, https://doi.org/10.5194/acp-18-4657-2018, 2018.

Sutanudjaja, E. H., van Beek, R., Wanders, N., Wada, Y., Bosmans, J. H. C., Drost, N., van der Ent, R. J., de Graaf, I. E. M., Hoch, J. M., de Jong, K., Karssenberg, D., López López, P., Peßenteiner, S., Schmitz, O., Straatsma, M. W., Vannametee, E., Wisser, D., and Bierkens, M. F. P.: PCR-GLOBWB 2: a 5 arcmin global hydrological and water resources model, Geosci. Model Dev., 11, 2429–2453, https://doi.org/10.5194/gmd-11-2429-2018, 2018.

Taddese, G., Sonder, K., and Peden, D.: The water of the Awash River basin: a future challenge to Ethiopia, ILRI, Addis Ababa, 2009.

Tadese, M. T., Kumar, L., Koech, R., and Zemadim, B.: Hydro-climatic variability: a characterisation and trend study of the Awash River Basin, Ethiopia, Hydrology, 6, 35, https://doi.org/10.3390/hydrology6020035, 2019.

Tarkegn, G. B. and Jury, M. R.: Changes in the seasonality of Ethiopian highlands climate and implications for crop growth, Atmosphere, 11, 892, https://doi.org/10.3390/atmos11090892, 2020.

Taye, M. T., Dyer, E., Hirpa, F. A., and Charles, K.: Climate change impact on water resources in the Awash basin, Ethiopia, Water, 10, 1560, https://doi.org/10.3390/w10111560, 2018.

Teku, D. and Eshetu, S.: Impact of climatic variabilities and extreme incidences on the physical environment, public health, and people's livelihoods in Ethiopia, Front. Clim., 6, 1435 138, https://doi.org/10.3389/fclim.2024.1435138, 2024.

Terray, P., Delecluse, P., Labattu, S., et al.: Sea surface temperature associations with the late Indian summer monsoon, Climate Dynamics, 21, 593–618, https://doi.org/10.1007/s00382-003-0354-0, 2003.

Thorncroft, C. D. and Hoskins, B. J.: An idealized study of African easterly waves. I: A linear view, Quarterly Journal of the Royal Meteorological Society, 120, 953–982, https://doi.org/10.1002/qj.49712051809, 1994.

Tierney, J. E., Ummenhofer, C. C., and DeMenocal, P. B.: Past and future rainfall in the Horn of Africa, Sci. Adv., 1, e1500 682, https://doi.org/10.1126/sciadv.1500682, 2015.

Tilahun, G. A., Gebremariam, E., and Desta, H.: Analysis of land use land cover changes and population dynamics in Awash River Basin (ARB), Ethiopia using GIS and remote sensing, Sci. Rep., 15, 34 017, https://doi.org/10.1038/s41598-025-12824-8, 2025.

Ting, M., Kushnir, Y., Seager, R., and Li, C.: Robust features of Atlantic multi-decadal variability and its climate impacts, Geophysical Research Letters, 38, L17 705, https://doi.org/10.1029/2011GL048712, 2011.

Tufa, Z. and Goshel, C.: Evaluation of ENSO impact on surface water storage of Awash River Basin in Ethiopia, J. Earth Sci. Clim. Change, 14, 2023.

United Nations: World Population Prospects 2022: Data Sources, 2022.

Varotsos, C. A., Tzanis, C. G., and Sarlis, N. V.: On the progress of the 2015–2016 El Niño event, Atmospheric Chemistry and Physics, 16, 2007–2011, https://doi.org/10.5194/acp-16-2007-2016, 2016.

Vicente-Serrano, S. M., Beguería, S., Gimeno, L., Eklundh, L., Giuliani, G., Weston, D., El Kenawy, A., López-Moreno, J. I., Nieto, R., Ayenew, T., et al.: Challenges for drought mitigation in Africa: The potential use of geospatial data and drought information systems, Appl. Geogr., 34, 471–486, https://doi.org/10.1016/j.apgeog.2012.02.001, 2012.

Viste, E., Korecha, D., and Sorteberg, A.: Recent drought and precipitation tendencies in Ethiopia, Theor. Appl. Climatol., 112, 535–551, https://doi.org/10.1007/s00704-012-0746-3, 2013.

Vizy, E. K. and Cook, K. H.: Connections between the summer east African and Indian rainfall regimes, Journal of Geophysical Research, 108, 4510, https://doi.org/10.1029/2003JD003452, 2003.

Wedajo, G. K., Muleta, M. K., and Awoke, B. G.: Performance evaluation of multiple satellite rainfall products for Dhidhessa River Basin (DRB), Ethiopia, Atmos. Meas. Tech., 14, 2299–2316, https://doi.org/10.5194/amt-14-2299-2021, 2021.

Williams, A. P. and Funk, C.: A westward extension of the warm pool leads to a westward extension of the Walker circulation, drying eastern Africa, Clim. Dyn., 37, 2417–2435, https://doi.org/10.1007/s00382-010-0984-y, 2011.

Williams, A. P., Funk, C., Michaelsen, J., et al.: Recent summer precipitation trends in the Greater Horn of Africa and the emerging role of Indian Ocean sea surface temperature, Climate Dynamics, 39, 2307–2328, https://doi.org/10.1007/s00382-011-1222-y, 2012.

Wolde-Georgis, T.: El Niño and Drought Early Warning in Ethiopia, https://ssrn.com/abstract=1589710, 1997.

Wongchuig, S., Papa, F., Fleischmann, A. S., et al.: Recent significant drying in Central Congo Basin linked to weakened Walker circulation and warmer Atlantic, npj Climate and Atmospheric Science, 8, 344, https://doi.org/10.1038/s41612-025-01225-3, 2025.

World Bank Group: World Bank Open Data, https://data.worldbank.org, 2023.

Xiao, D. and Ren, H.: A regime shift in North Pacific annual mean sea surface temperature in 2013/14, Frontiers in Earth Science, 10, 987 349, https://doi.org/10.3389/feart.2022.987349, 2023.

Yadav, R. K.: The recent trends in the Indian summer monsoon rainfall, Environment, Development and Sustainability, 27, 13 565–13 579, https://doi.org/10.1007/s10668-024-04488-7, 2025.

Yang, W., Seager, R., Cane, M. A., and Lyon, B.: The East African long rains in observations and models, J. Clim., 27, 7185–7202, https://doi.org/10.1175/JCLI-D-13-00447.1, 2014.

Yu, L., Zhong, S., Vihma, T., Sui, C., and Sun, B.: A change in the relation between the Subtropical Indian Ocean Dipole and the South Atlantic Ocean Dipole indices in the past four decades, Atmospheric Chemistry and Physics, 23, 345–353, https://doi.org/10.5194/acp-23-345-2023, 2023.

Zhang, W., Zhou, T., Ye, W., et al.: A year marked by extreme precipitation and floods: Weather and climate extremes in 2024, Adv. Atmos. Sci., 42, 1045–1063, https://doi.org/10.1007/s00376-025-4540-4, 2025.

Zhang, Y., Wallace, J. M., and Battisti, D. S.: ENSO-like Interdecadal Variability: 1900–93, J. Clim., 10, 1004–1020, https://doi.org/10.1175/1520-0442(1997)010<1004:ELIV>2.0.CO;2, 1997.

Zhao, G., Li, Y., Zhou, L., et al.: Evaporative water loss of 1.42 million global lakes, Nat. Commun., 13, 3686, https://doi.org/10.1038/s41467-022-31125-6, 2022.

https://doi.org/10.5194/egusphere-2026-3724
Preprint. Discussion started: 27 July 2026

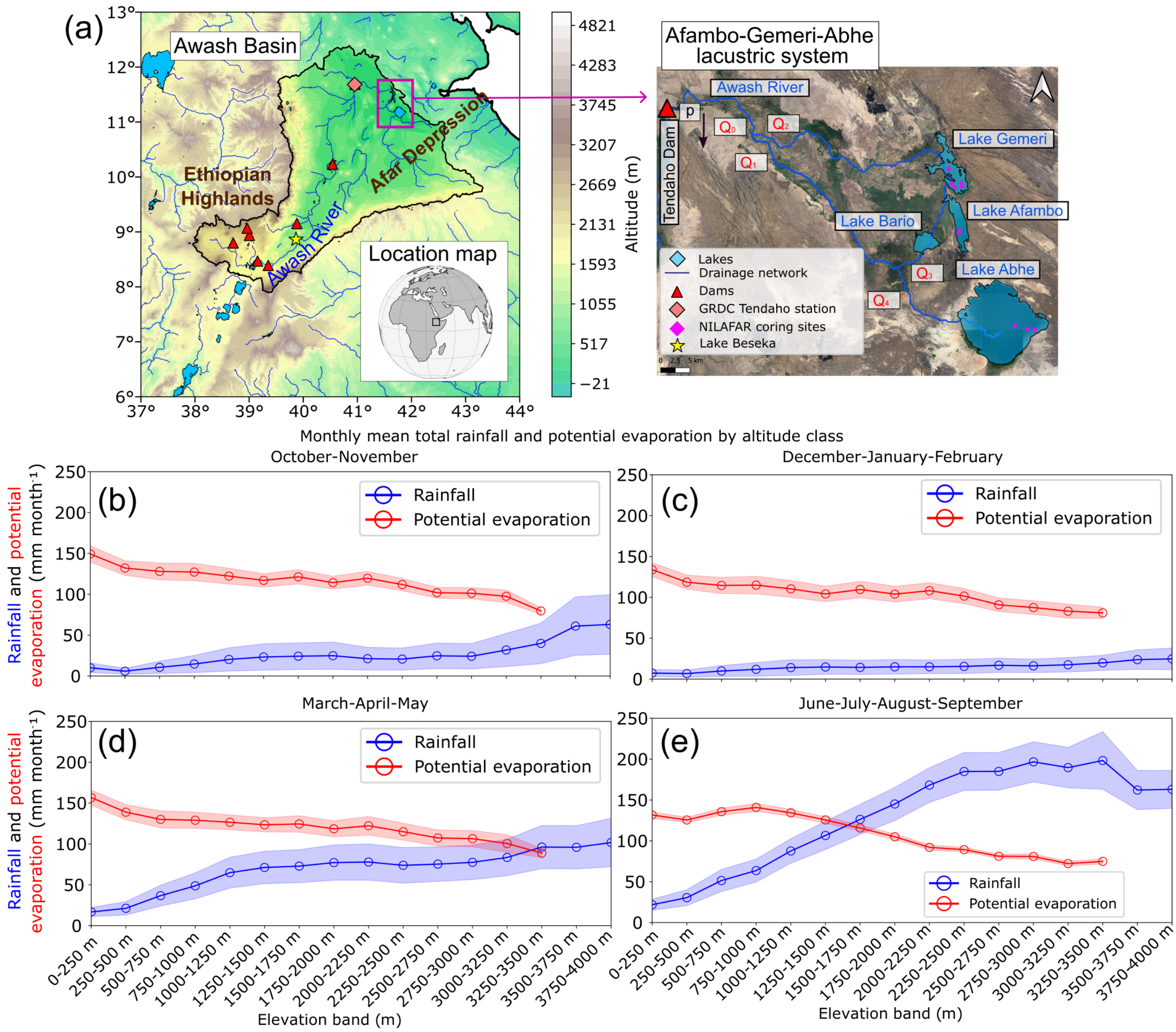

Figure 1. (a) Location of the Awash River Basin, view of the Abhe–Afambo–Gemeri lake system and schematic representation of the flow partitioning used in the lake model (satellite image from Sentinel-2). Topography derived from the Shuttle Radar Topography Mission (SRTM; Farr et al., 2007) is shown as shaded relief (m, a.s.l.), and river and lake polygons are from the HydroRIVERS (Lehner and Grill, 2021) and HydroLAKES (Messager et al., 2016) databases. (b–e) Climatology of precipitation and total potential evaporation as a function of elevation for the period 1981–2024: (b) October–November, (c) December–February, (d) March–May, and (e) June–September. Shading indicates ±1 standard deviation. Precipitation and potential evaporation data are derived from CHIRPSv2 (Funk et al., 2015) and GLEAMv4.2a (Miralles et al., 2025), respectively.

https://doi.org/10.5194/egusphere-2026-3724
Preprint. Discussion started: 27 July 2026

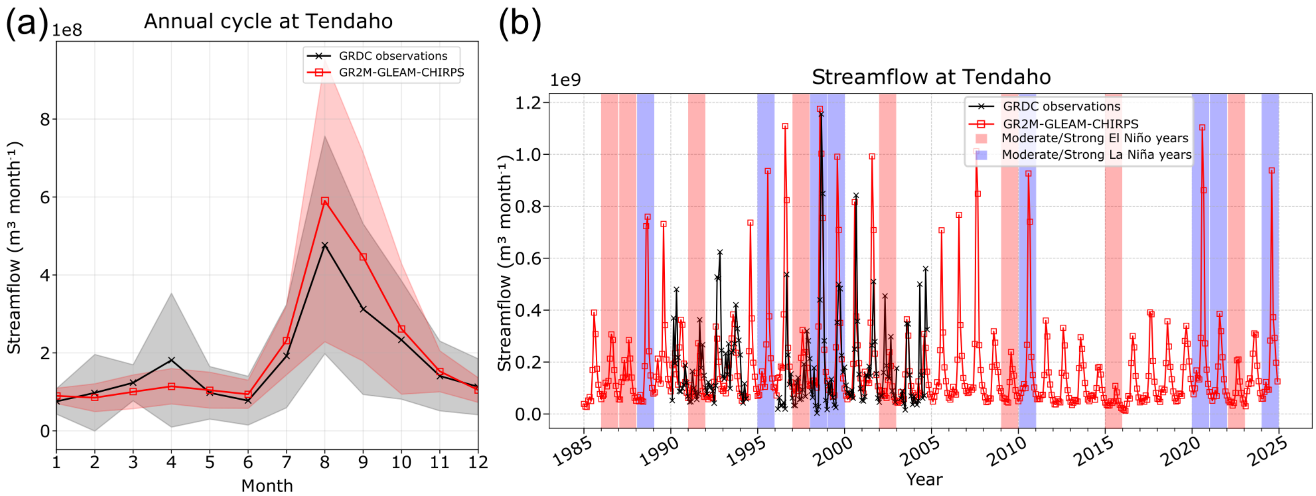

Figure 2. (a) Mean annual cycle of observed and simulated discharge at the Tendaho station for the period 1990–2004, based on simulations with the GR2M model. Shaded areas indicate the variability of monthly accumulated discharge (±1 standard deviation; m^3 month^{-1}). (b) Time series of observed and simulated monthly discharge at Tendaho (m^3 month^{-1}). Moderate and strong El Niño (red) and La Niña (blue) years are indicated based on the Oceanic Niño Index (ONI) from the National Centers for Environmental Prediction–National Oceanic and Atmospheric Administration (NCEP–NOAA; available at https://psl.noaa.gov/data/timeseries/month/, last access 29 April 2026).

https://doi.org/10.5194/egusphere-2026-3724
Preprint. Discussion started: 27 July 2026

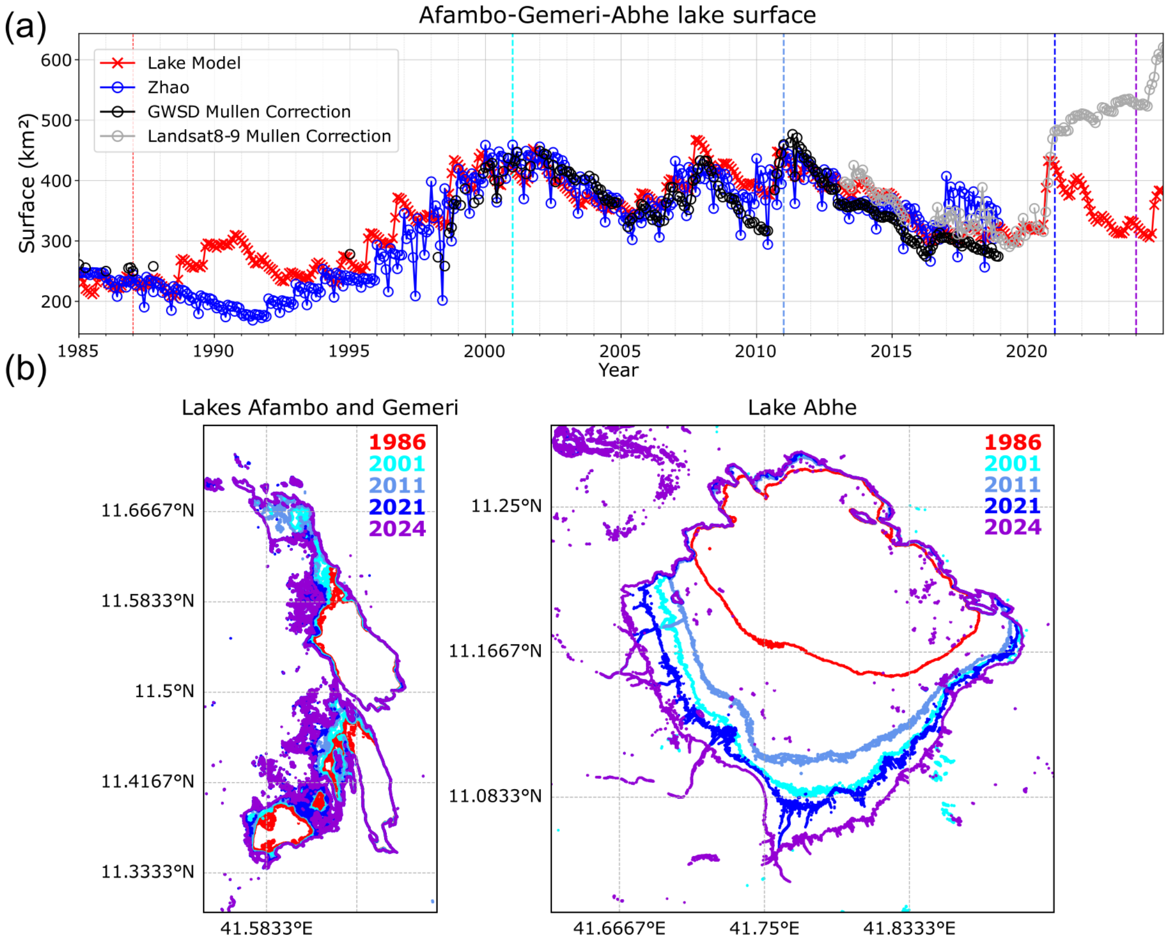

Figure 3. (a) Combined surface area of the Afambo–Gemeri–Abhe lake system derived from the corrected Global Surface Water Dataset (GSWD), extended to 2025 using Landsat 8–9 imagery, the reconstruction of Zhao et al. (2022), and GR2M-lake model simulations. Vertical lines indicate the selected years for which lake extent isolines are shown in panel (b). (b) Spatial extent of the Afambo–Gemeri–Abhe lake system for selected years (1986, 2001, 2011, 2021, and 2024), represented as isolines delineating the area inundated during at least 90% of each year, derived from corrected GSWD imagery. The progression of isolines illustrates the gradual expansion of the lake system over the past four decades.

https://doi.org/10.5194/egusphere-2026-3724
Preprint. Discussion started: 27 July 2026

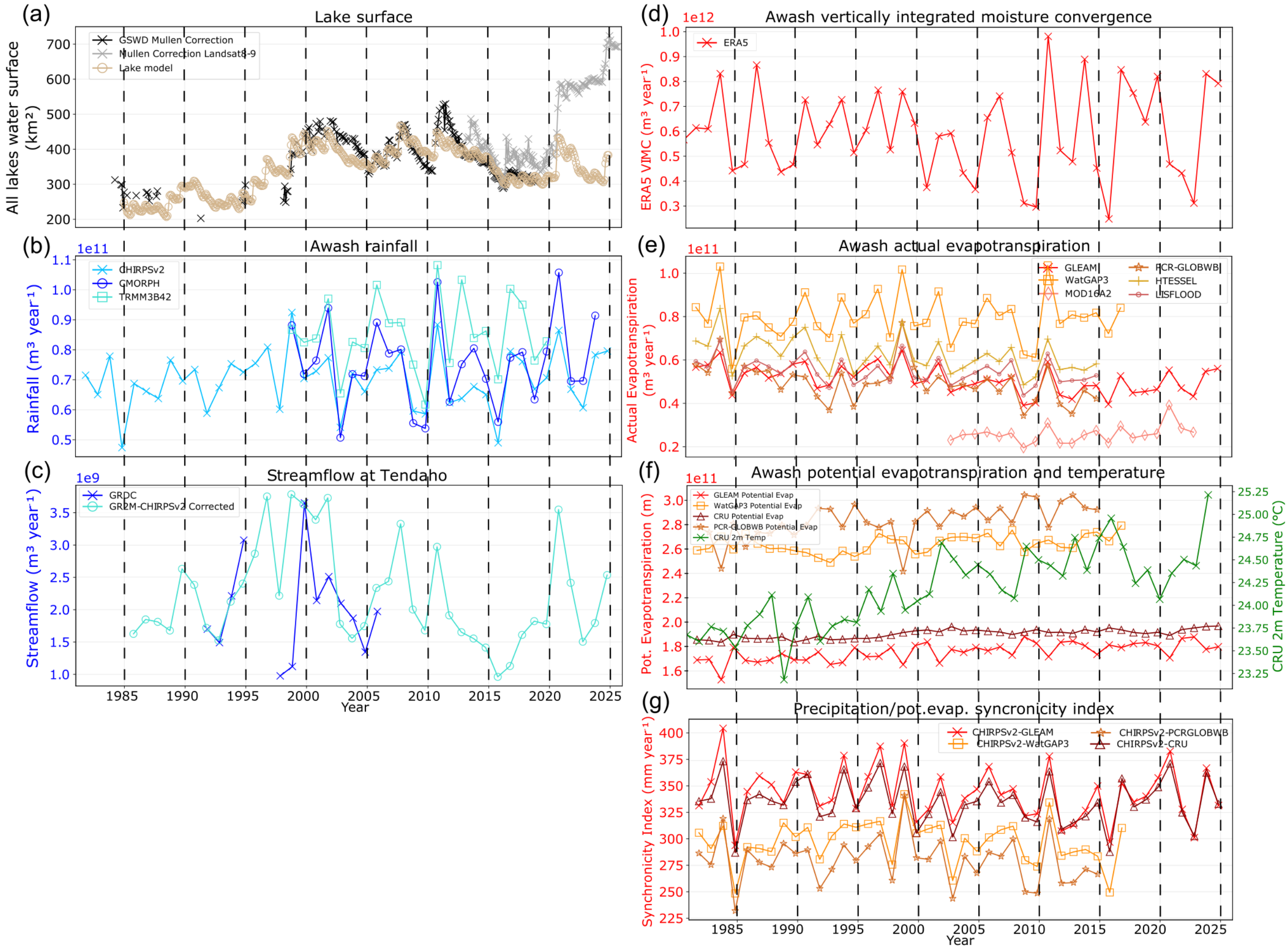

Figure 4. (a)Time series of the total surface area (km^2) of Lakes Abhe, Afambo, and Gemeri, observed from GSWD and Landsat 8–9 data and simulated using the lake model. (b) Time series of the total annual rainfall from the CHIRPSv2, CMORPH, and TRMM3B42 products ($m^3\,year^{-1}$). (c) Time series of the annual cumulative discharge at Tendaho, observed (GRDC) and simulated (GR2M) ($m^3\,year^{-1}$). (d) Time series of the vertically integrated moisture convergence derived from ERA5 ($m^3\,year^{-1}$). (e) Time series of the actual evapotranspiration from GLEAM v4.2a, WaterGAP3, HTESSEL, LISFLOOD, PCR-GLOBWB and MOD16A2 ($m^3\,year^{-1}$); (f) Time series of the potential evapotranspiration from GLEAM v4.2a, WaterGAP3, PCR-GLOBWB, and CRU v4.09 ($m^3\,year^{-1}$), and basin-averaged mean annual surface temperature from CRU TS v4.09 (°C); (g) Time series of the rainfall–potential evaporation synchronicity index proposed by Andréassian et al. (2025) ($mm\,year^{-1}$). Volumes corresponding to rainfall, atmospheric moisture convergence, actual evaporation, and potential evaporation were spatially aggregated over the entire Awash Basin and integrated over hydrological years extending from October to September.

https://doi.org/10.5194/egusphere-2026-3724
Preprint. Discussion started: 27 July 2026

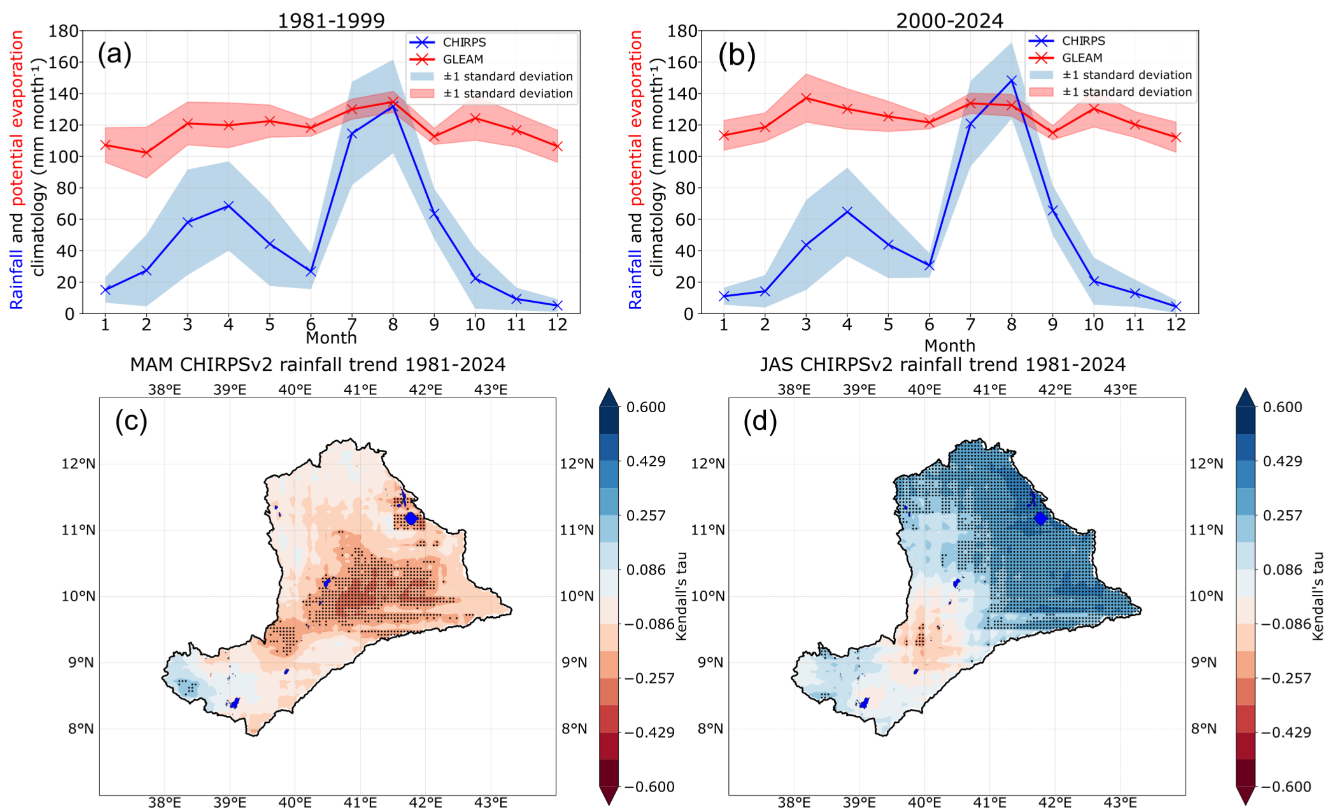

Figure 5. Annual cycle of rainfall (CHIRPSv2) and potential evaporation (GLEAM v4.2a) ($\mathrm{mm\ month}^{-1}$) for the periods (a) 1981–1999 and (b) 2000–2024. Shaded areas represent interannual variability (± 1 standard deviation). Panels (c) and (d) show spatial trends in accumulated rainfall over the Awash Basin during March–April–May (MAM) and July–August–September (JAS) over 1981–2024, respectively, based on CHIRPSv2 and expressed as Kendall's τ coefficients. Black dots indicate grid cells with statistically significant trends at the 95% confidence level ($p < 0.05$) using a Mann–Kendall test.

https://doi.org/10.5194/egusphere-2026-3724
Preprint. Discussion started: 27 July 2026

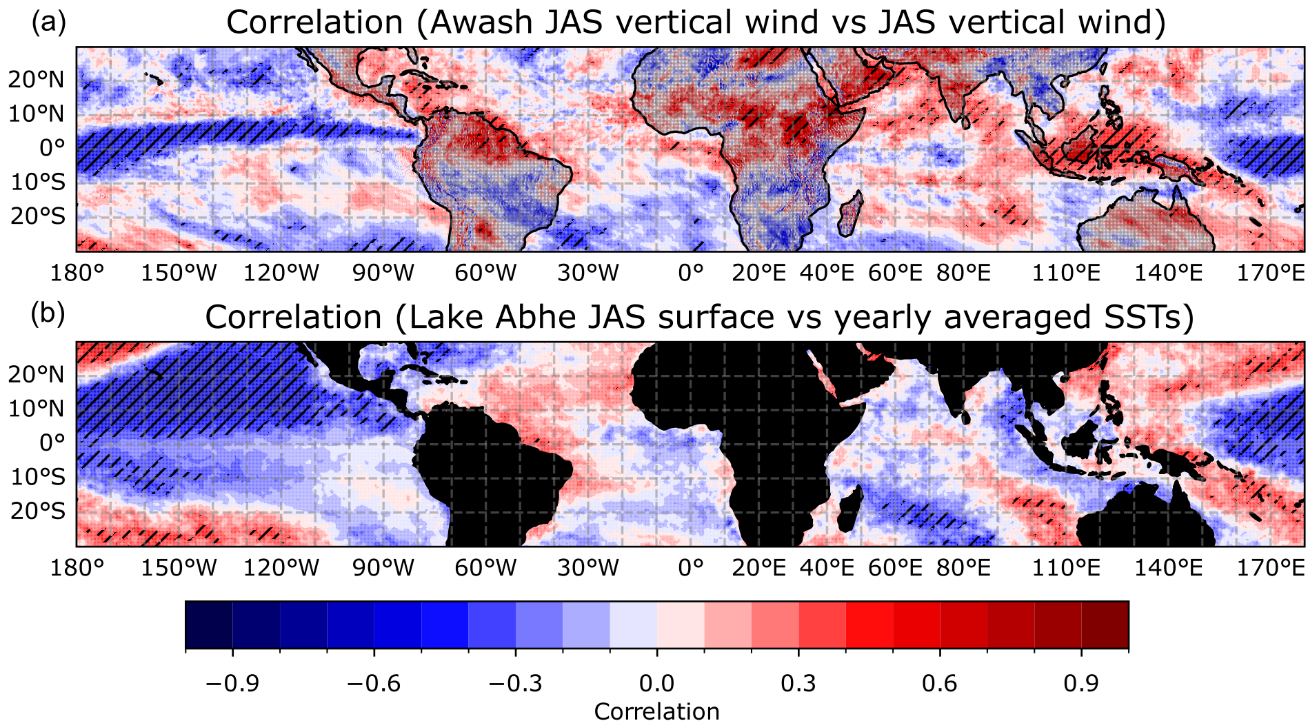

Figure 6. (a) Correlation between JAS anomalies of ERA5 pressure vertical velocity at 500 hPa (ω_{500}) averaged over the Awash Basin and JAS ω_{500} anomalies over the tropics (30°S–30°N). (b) Correlation between JAS anomalies in Lake Abhe surface area (Zhao et al., 2022) and annual mean sea surface temperature anomalies from OISSTv2.1. Linear trends were removed at each grid cell prior to the correlation analysis. Grid cells with correlations significant at the 95% confidence level are hatched.

https://doi.org/10.5194/egusphere-2026-3724
Preprint. Discussion started: 27 July 2026

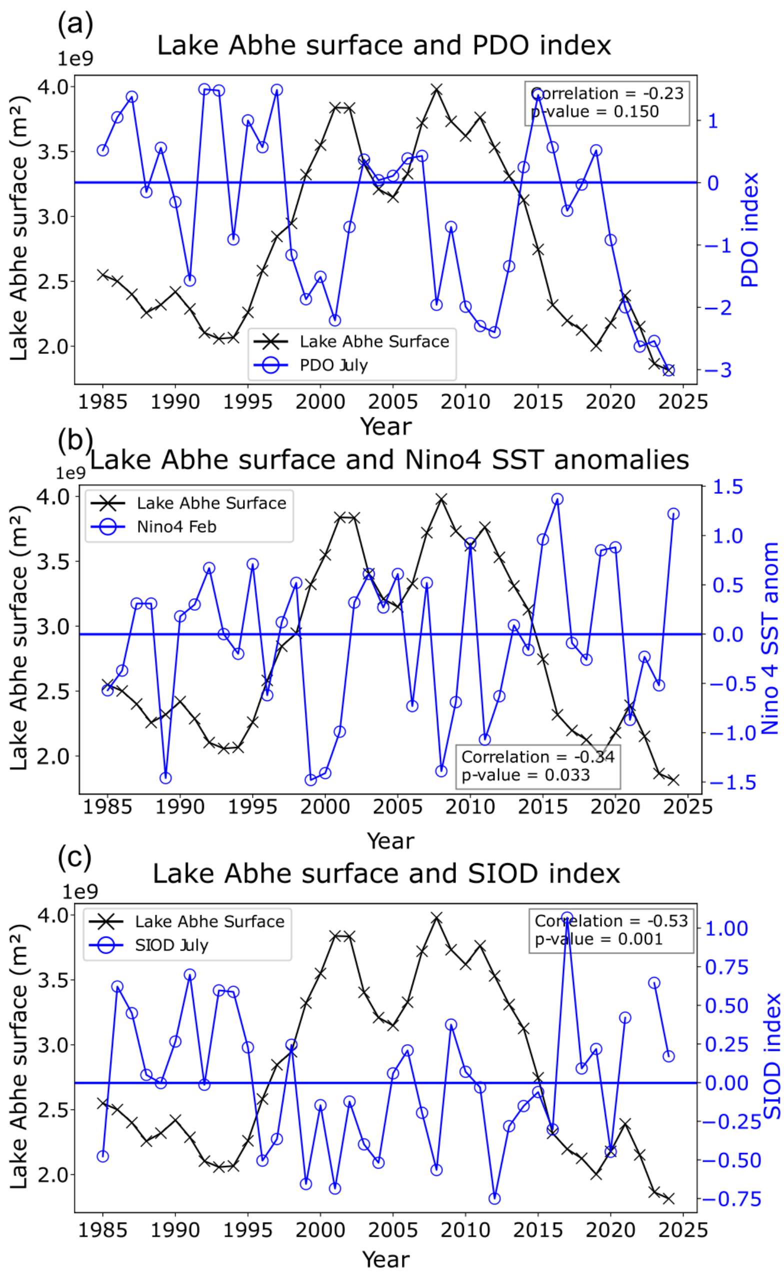

Figure 7. Time series of detrended annual lake surface area of Lake Abhe, simulated by the lake model, and (a) the Pacific Decadal Oscillation (PDO) index, (b) El Niño 4 SST anomalies, both from the NOAA National Centers for Environmental Information (https://www.ncei.noaa.gov/access/monitoring/pdo/; last access 12 February 2026), and (c) the Subtropical Indian Ocean Dipole (SIOD) index, computed as the difference between detrended monthly SST anomalies averaged over the western (55°–58°E, 32°–15°S) and eastern (92°–110°E, 32°–15°S) subtropical Indian Ocean (NOAA OI SST v2.1). For PDO and SIOD (El Niño 4) indices, July (February) values are shown, corresponding to the month of highest correlation with lake surface area. Pearson correlation coefficients are indicated in each panel.

https://doi.org/10.5194/egusphere-2026-3724
Preprint. Discussion started: 27 July 2026

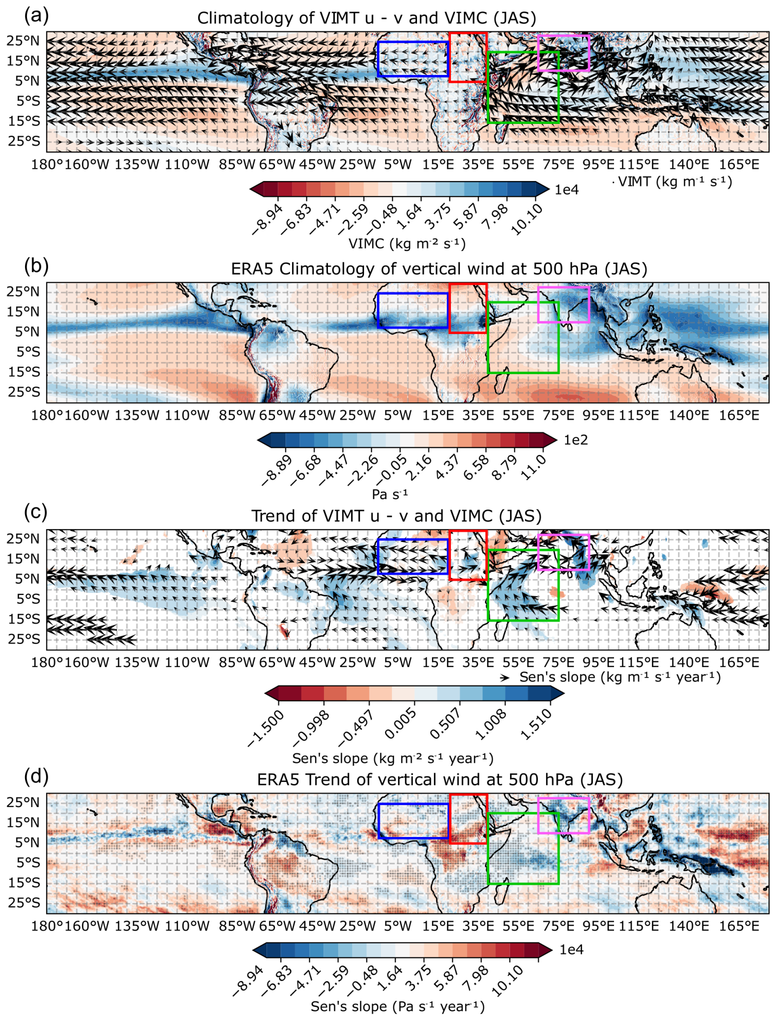

Figure 8. Climatological fields of (a) vertically integrated moisture transport (vectors, $\mathrm{kg\,m^{-1}s^{-1}}$) and vertically integrated moisture convergence (shading, $\mathrm{kg\,m^{-2}s^{-1}}$), and (b) vertical velocity at 500 hPa ($\mathrm{Pa\,s^{-1}}$). Linear trends estimated using Sen's slope for (c) vertically integrated moisture transport (vectors, $\mathrm{kg\,m^{-1}s^{-1}year^{-1}}$) and vertically integrated moisture convergence (shading, $\mathrm{kg\,m^{-2}s^{-1}year^{-1}}$), and (d) vertical velocity at 500 hPa ($\mathrm{Pa\,s^{-1}year^{-1}}$. Fields are derived from ERA5 for the period 1979–2024 during JAS. Only statistically significant trends at the 95% confidence level are shown in (c). Grid points with significant trends (95% confidence level) in vertical velocity are indicated by gray dots in (d) using a Mann–Kendall test. Blue, red, green, and pink boxes indicate regions associated with the African Easterly Jet (AEJ), the northern branch of the Hadley circulation, the Somali Jet, and convection over India, respectively.

https://doi.org/10.5194/egusphere-2026-3724
Preprint. Discussion started: 27 July 2026

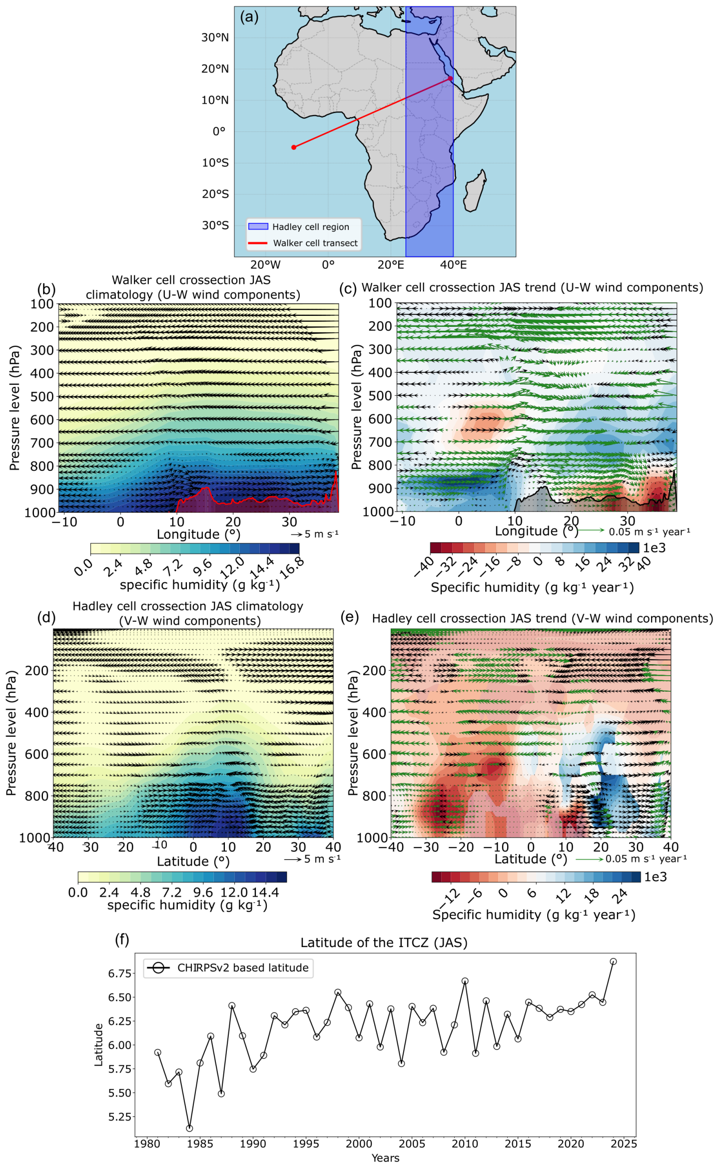

Figure 9. (a) Reference map showing the transect used to examine the zonal overturning (Walker-type) circulation (red line) and the domain used to analyze the regional meridional (Hadley-type) circulation (blue box). (b) Climatology and (c) linear trends of zonal and vertical wind components and specific humidity along the transect. (d) Climatology and (e) linear trends of meridional and vertical wind components and specific humidity, zonally averaged within the boxed region. (f) Time series of the ITCZ latitude within the blue domain, following the methodology of Adam et al. (2016). Wind trends significant at the 95% confidence level are shown in green. For specific humidity, statistically significant trends (95%) are displayed with full-color shading, whereas non-significant trends are shown with reduced opacity using a Mann–Kendall test. Red and black lines in (b) and (c) indicate topography along the transect. Wind and humidity fields are derived from ERA5 (1979–2024), and rainfall used to determine the ITCZ latitude is from CHIRPSv2 (1981–2024). All climatologies and trends correspond to the JAS season.

https://doi.org/10.5194/egusphere-2026-3724
Preprint. Discussion started: 27 July 2026

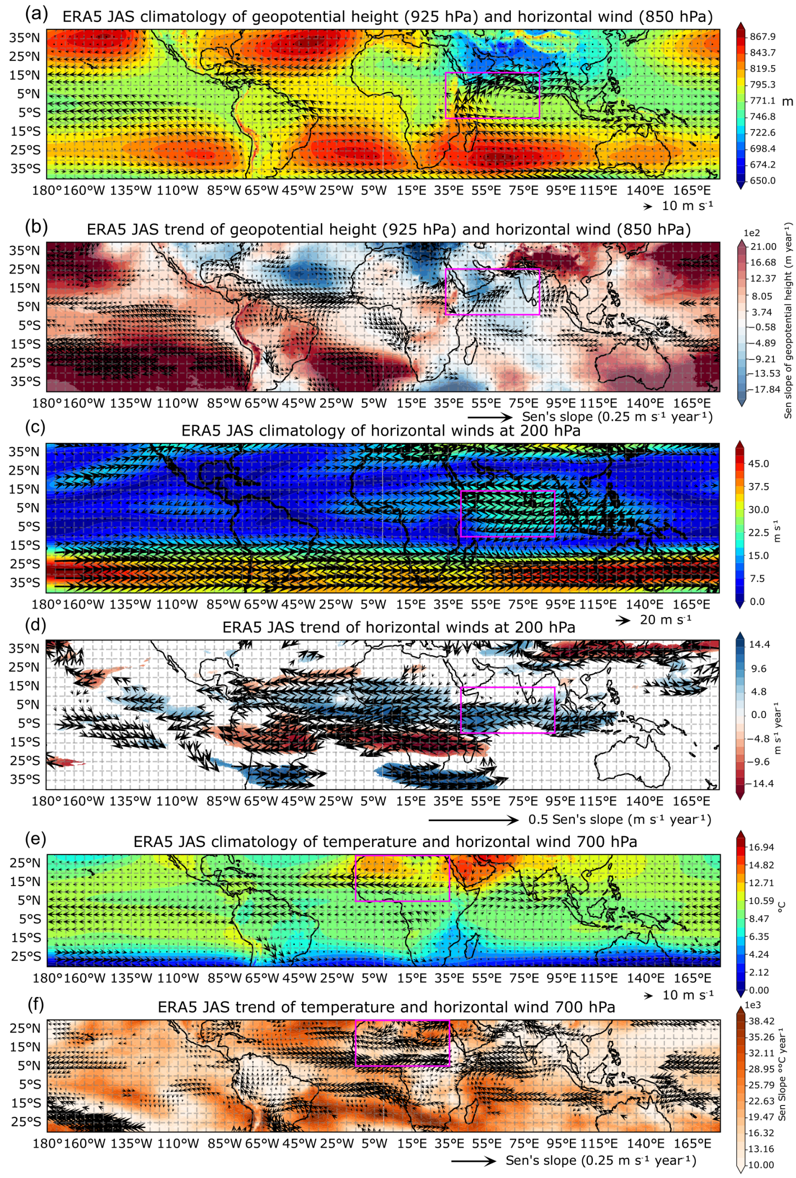

Figure 10. JAS climatology and linear trends (1979–2024) of atmospheric circulation associated with the Somali Jet, Tropical Easterly Jet (TEJ), and African Easterly Jet (AEJ) from the ERA5 reanalysis. Panels (a–b) depict the Somali Jet, showing (a) climatological geopotential height at 925 hPa (shading; m) and horizontal winds at 850 hPa (vectors; $\mathrm{m\,s^{-1}}$), and (b) their corresponding linear trends ($\mathrm{m\,year^{-1}}$ and $\mathrm{m\,s^{-1}\,year^{-1}}$, respectively). For geopotential height trends, statistically significant values at the 95% confidence level are shown with full-color shading, whereas non-significant values are displayed with reduced opacity. Panels (c–d) depict the TEJ, showing (c) climatological wind speed (shading; $\mathrm{m\,s^{-1}}$) and horizontal wind vectors at 200 hPa, and (d) their linear trends ($\mathrm{m\,s^{-1}\,year^{-1}}$). Panels (e–f) depict the AEJ, showing (e) climatological air temperature (shading) and horizontal wind vectors at 700 hPa, and (f) their linear trends. For the AEJ, only trends significant at the 95% confidence level according to the Mann–Kendall test are displayed. The magenta boxes indicate the regions used to characterize each atmospheric jet.

https://doi.org/10.5194/egusphere-2026-3724
Preprint. Discussion started: 27 July 2026

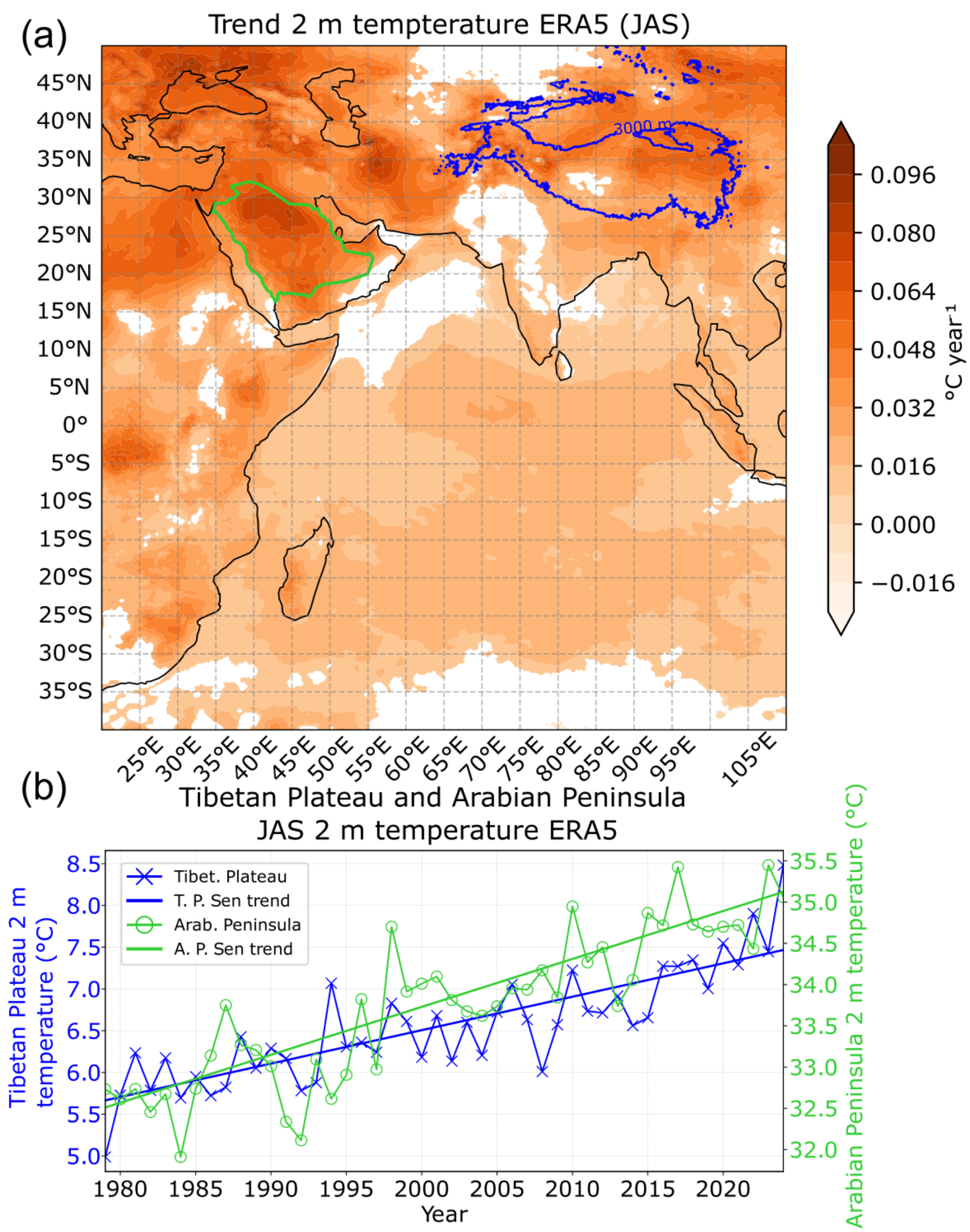

Figure 11. (a) Spatial distribution of JAS (July–August–September) linear temperature trends at 2 m above the surface berween 20°E–110°E, 40°S–50°N for the period 1979–2025, derived from ERA5 reanalysis. Trends are expressed as Sen's slopes ($°C\,year^{-1}$). Only grid cells with statistically significant trends (Mann–Kendall test, $p < 0.05$) are shown. The blue and green lines delineate the boundaries of the Tibetan Plateau and Saudi Arabia, respectively, used as a reference regions to characterize the warming signal over both regions. (b) Annual JAS-mean 2 m temperature averaged over Tibetan Plateau and Saudi Arabia for the period 1979–2025, derived from ERA5 reanalysis. The trend line and corresponding Sen's slope ($°C\,year^{-1}$) are shown.

https://doi.org/10.5194/egusphere-2026-3724
Preprint. Discussion started: 27 July 2026

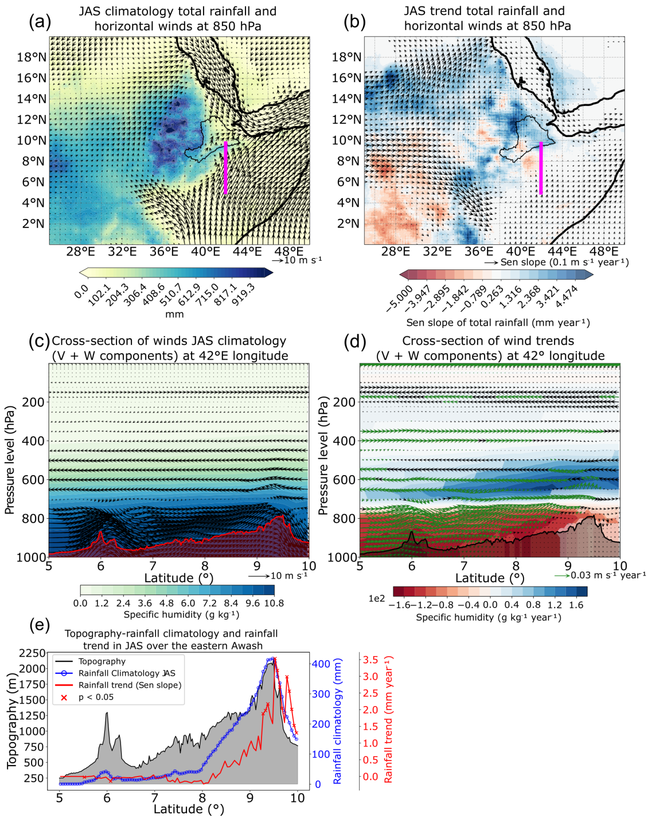

Figure 12. (a) Climatological JAS accumulated rainfall (shading; mm) and horizontal winds at 850 hPa (vectors; $\mathrm{m\,s^{-1}}$) over northeast Africa. (b) Linear trends in accumulated rainfall (shading; $\mathrm{mm\,year^{-1}}$) and horizontal winds at 850 hPa (vectors; $\mathrm{m\,s^{-1}\,year^{-1}}$). The Awash Basin is outlined in panels (a)–(b), and the magenta line indicates the location of the cross-section shown in panels (c)–(d). Only grid cells with statistically significant trends at the 95% confidence level are shown in panel (b), based on a Mann–Kendall test. (c) Climatological meridional–vertical circulation (vectors; $\mathrm{m\,s^{-1}}$) and specific humidity (shading; $\mathrm{g\,kg^{-1}}$) along a 43°E transect between 5°N and 10°N during JAS. (d) Linear trends in meridional–vertical circulation (vectors; $\mathrm{m\,s^{-1}\,year^{-1}}$) and specific humidity (shading; $\mathrm{g\,kg^{-1}\,year^{-1}}$) along the same cross-section. Red and black lines in (c) and (d) indicate local topography. Green vectors in (d) highlight statistically significant trends at the 95% confidence level. For specific humidity, significant trends are shown with full-color shading, while non-significant values are displayed with reduced opacity. (e) Topography (black line), climatological rainfall (blue line), and linear rainfall trends (red line) along the transect; crosses indicate locations where rainfall trends are significant at the 95% confidence level (Mann–Kendall test). Rainfall data are from CHIRPS v2 (1981–2024), and all other variables are from ERA5 (1979–2024).

https://doi.org/10.5194/egusphere-2026-3724
Preprint. Discussion started: 27 July 2026

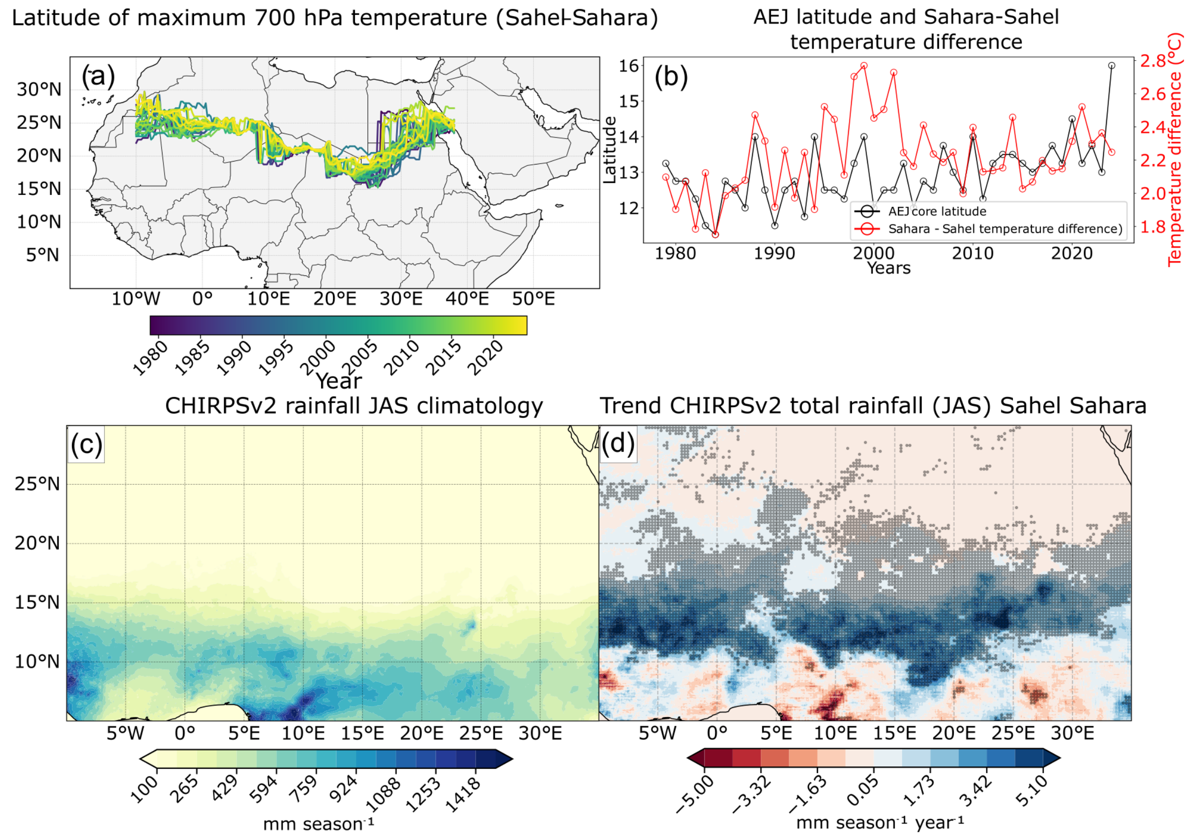

Figure 13. (a) Latitude of maximum air temperature at 700 hPa for each longitude within the region 10°–38°E and 4°–30°N for each year during 1979–2024. (b) Time series of the latitudinal position of the AEJ core (defined as the latitude of maximum easterly zonal wind at 700 hPa within 5°S–30°N and 10°W–30°E; black line) and the meridional temperature gradient at 700 hPa between the Sahara (15°–20°N, 10°W–30°E) and the Sahel (5°–10°N, 10°W–30°E) (red line). (c) Climatology and (d) linear trends of accumulated JAS precipitation from CHIRPSv2 for the period 1981–2024. Trends significant at the 95% confidence level are indicated by black dots using a Mann–Kendall test.

https://doi.org/10.5194/egusphere-2026-3724
Preprint. Discussion started: 27 July 2026

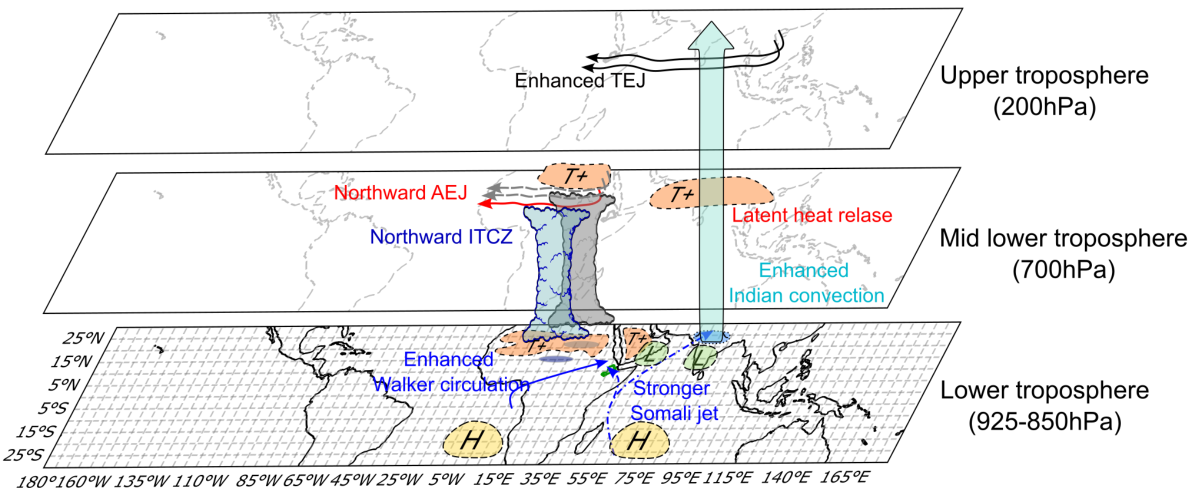

Figure 14. Schematic representation of trends in large-scale atmospheric processes associated with rainfall variability in the Awash Basin during the July–August–September (JAS) wet season. The letters H and L indicate positive and negative trends in lower-tropospheric pressure, respectively. T+ denotes tropospheric warming. Blue arrows indicate low-level atmospheric circulation. Red and black arrows show changes in the African Easterly Jet (AEJ) and the Tropical Easterly Jet, respectively. Gray arrows and gray cloud indicate the northward displacement of the AEJ and the Intertropical Convergence Zone (ITCZ), respectively.

https://doi.org/10.5194/egusphere-2026-3724
Preprint. Discussion started: 27 July 2026

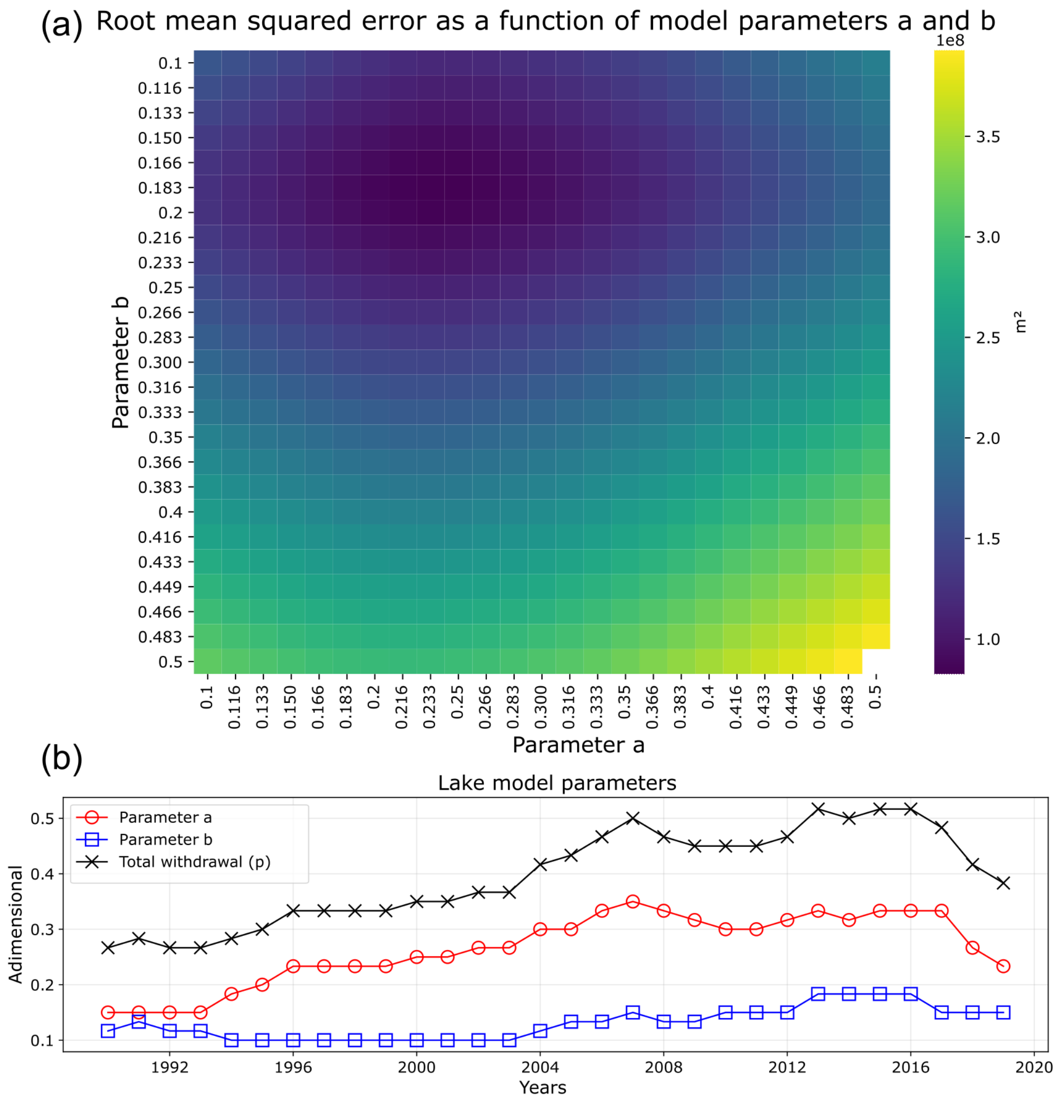

Figure A1. (a) Example of the estimation of lake model parameters a and b using the complete period 1985–2024. (b) Time series of the lake model parameters a, b, and p. Parameter values are plotted at the midpoint of each 10-year moving window; for example, parameters estimated for the 1985–1995 window are plotted at 1990.